

# Precision Passive Alignment of Wafers

by

**Alexis Christian Weber**

B. S. Mechanical and Electrical Engineering (1998)  
Instituto Tecnológico y de Estudios Superiores de Monterrey, Mexico

Submitted to the Department of Mechanical Engineering  
in Partial Fulfillment of the Requirements for the Degree of

Master of Science in Mechanical Engineering

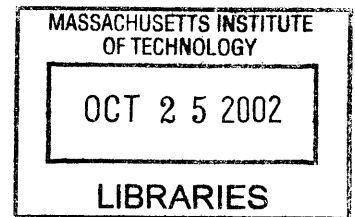
at the

MASSACHUSETTS INSTITUTE OF TECHNOLOGY

February, 2002

© 2002 Massachusetts Institute of Technology.  
All Rights Reserved

**BARKER**



Signature of Author .....

.....  
Department of Mechanical Engineering  
February, 2002

Certified by ..

.....  
Alexander H. Slocum  
Professor, Mechanical Engineering  
Thesis Supervisor

Accepted by .....

.....  
Ain A. Sonin  
Chairman, Mechanical Engineering Graduate Committee



# Precision Passive Alignment of Wafers

by

ALEXIS CHRISTIAN WEBER

Submitted to the Department of Mechanical Engineering  
on February 20, 2002 in Partial Fulfillment of the  
Requirements for the Degree of Master of Science in  
Mechanical Engineering

## ABSTRACT

Several macro-scale bench level experiments were carried out to evaluate the alignment repeatability that can be obtained through the elastic averaging principle. Based on these results, a precision passive alignment technique for wafer bonding application was developed. Wafer integral features that allow two stacked wafers to self-align were designed, fabricated and tested for wafer alignment repeatability and accuracy. Testing has demonstrated sub-micrometer repeatability and accuracy can be held using the proposed technique on 4 inch wafers.

Passive alignment of the wafers is achieved when convex pyramids, supported on flexural cantilevers, and concave v-grooves patterned on the edges of the wafer engage and are preloaded. A silicon cantilever beam flexure between one of the wafers and the pyramid provides compliance to the coupling to avoid strain on the wafers and allows the surfaces of the wafers to mate.

Both the concave coupling features and the convex coupling features are bulk micromachined through wet anisotropic etch (KOH). The convex features are then release etched through a back-side deep reactive ion etch (DRIE).

As part of the fabrication process development, tests were performed to optimize the convex corner compensating mask structures needed to create the pyramid shaped convex coupling structures.

Testing has shown that patterning two pairs of features on each of the four sides of the wafer is enough to achieve sub-micrometer repeatability.

Thesis Supervisor: Alexander H. Slocum  
Title: Professor of Mechanical Engineering



# ACKNOWLEDGMENTS

I want to thank foremost Prof. Slocum for his guidance throughout this research project, and for his continuous support throughout my time at MIT. His energy and passion for engineering, have made me grow academically, personally and professionally.

To everybody at the Precision Engineering Research Group, I thank sincerely for their friendship and for the help they never hesitated in providing. I am honored to have shared lab space, interesting conversations and long hours of work with you.

Thanks to the MTL staff and users for their continuous advice. I am particularly grateful to Dr. Vicky Diadiuk, Gwen Donahue, Kurt Broderick, Paul Garth, Paudley Zamora, Dennis Ward and Ravi Khanna for their guidance and help.

During my time at MIT, I was generously sponsored by a fellowship from Delphi Automotive Systems. I am grateful to Mark Shost and the MTC staff, for believing in me. Thanks to Mark Shost for mentoring me throughout my graduate studies. I am grateful to Ivan Samalot, for having “pushed” me to come to MIT, as well as for his continuous, unconditional and unselfish support. Thanks to Albert Vega for helping me out with all the administrative issues. I am grateful to Enrique Calvillo for his help with the transition back to Mexico.

I am most grateful to my parents, for their love and support: gracias por todo! Thanks to my father, for giving me the passion for engineering: unvregessen die Gespraechen vor dem Kindergarten! Thanks to my best friends: Andreas and Walter: que sigamos siendo tan unidos como hasta ahora. Thanks to my "favorite" aunt and uncle, Babs & Donald, for their continuous support. I am grateful to my Grandparents, who taught us hard work and love for the adventure and the unknown: Euer Leben wird uns immer ein Vorbild sein.

A special thanks goes to Carissa, for the long hours working on problem sets, lab reports, and preparing for quizzes; thanks for the beautiful friendship, continuous support and for the shared dreams.



# TABLE OF CONTENTS

<b>ACKNOWLEDGMENTS</b> . . . . .	<b>5</b>
<b>TABLE OF CONTENTS</b> . . . . .	<b>7</b>
<b>LIST OF FIGURES</b> . . . . .	<b>9</b>
<b>LIST OF TABLES</b> . . . . .	<b>13</b>
<b>CHAPTER 1. INTRODUCTION</b> . . . . .	<b>15</b>
1.1 Background . . . . .	15
1.2 Motivation . . . . .	16
<b>CHAPTER 2. CURRENT WAFER AND MEMS ALIGNMENT PRINCIPLES</b> . . . . .	<b>17</b>
2.1 Wafer alignment through optical systems . . . . .	17
2.2 Passive alignment in Optical MEMS . . . . .	18
<b>CHAPTER 3. MACRO-SCALE PRECISION ALIGNMENT</b> . . . . .	<b>21</b>
3.1 Precision Machine Design Alignment Principles . . . . .	21
3.1.1 Kinematic Couplings . . . . .	22
3.1.2 Flexural Kinematic Couplings . . . . .	24
3.1.3 Elastic Averaging . . . . .	24
3.2 Elastic Averaging Bench Level Experiment . . . . .	26
3.2.1 Repeatability of a 2X4 Projection Lego™ block . . . . .	27
3.2.2 Repeatability and number of contact points . . . . .	31
<b>CHAPTER 4. DESIGN OF A WAFER-LEVEL PASSIVE ALIGNMENT COUPLING</b> . . . . .	<b>37</b>
4.1 Product values and goals . . . . .	37
4.2 Strategy selection . . . . .	38
4.2.1 Kinematic couplings . . . . .	38
4.2.2 Flexural kinematic couplings . . . . .	42
4.2.3 Elastic averaging . . . . .	42
4.2.4 Pinned joints . . . . .	43
4.3 Design constraints . . . . .	43
4.4 Concept selection . . . . .	44

4.5	Functional Requirements . . . . .	44
4.6	Design parameters . . . . .	44
4.7	Design layout . . . . .	45
4.8	Manufacturing considerations . . . . .	46
4.8.1	Groove / pyramid layout on wafer . . . . .	47
4.8.2	Principal etch planes of convex-cornered masked features in anisotropic etchants . . . . .	47
4.9	Design detailing . . . . .	49
<b>CHAPTER 5. MICROFABRICATION . . . . .</b>		<b>51</b>
5.1	Fabrication processes . . . . .	51
5.1.1	Concave coupling features . . . . .	52
5.1.2	Concave coupling features . . . . .	54
5.2	Process optimization: Convex corner compensating structures . . . . .	57
<b>CHAPTER 6. TESTING AND RESULTS . . . . .</b>		<b>63</b>
6.1	Testing sequence . . . . .	63
6.2	Determination of the measurement system noise . . . . .	65
6.3	Repeatability and accuracy results of passive wafer alignment . . . . .	65
6.4	Repeatability and accuracy as a function of number of contact points: the elastic averaging effect . . . . .	66
<b>CHAPTER 7. CONCLUSIONS AND FUTURE WORK . . . . .</b>		<b>71</b>
<b>REFERENCES . . . . .</b>		<b>73</b>
<b>Appendix A. Process Sequence . . . . .</b>		<b>77</b>
<b>Appendix B. Masks . . . . .</b>		<b>81</b>
<b>Appendix C. Experimental Results: CCCS . . . . .</b>		<b>85</b>
<b>Appendix D. Passive Wafer Alignment Test Data . . . . .</b>		<b>89</b>



# LIST OF FIGURES

Figure 3.3	Coupling arrangement to ensure stability (figure by A. H. Slocum, Design of three-groove kinematic couplings [9]) . . . . .	23
Figure 3.1	Three-groove kinematic coupling disassembled . . . . .	23
Figure 3.2	Three-groove kinematic coupling assembled . . . . .	23
Figure 3.4	Flexural kinematic coupling “Kinflex” (US patent 5,678,944 [10]) . . . . .	24
Figure 3.5	Circle divider (figure by W. R. Moore, Foundations of mechanical accuracy [12]) . . . . .	25
Figure 3.6	Curvic coupling disengaged (figure by W. R. Moore, Foundations of mechanical accuracy[12]) . . . . .	26
Figure 3.7	Curvic coupling engaged (figure by W. R. Moore, Foundations of mechanical accuracy[12]) . . . . .	26
Figure 3.8	Top view of 2x6 PP building block . . . . .	27
Figure 3.9	Bottom view of a 2x6 PP building block . . . . .	27
Figure 3.10	Cross-section at the interface of two blocks showing three line contact of every primary projection with adjacent secondary projections . . . . .	27
Figure 3.11	Measurement target for repeatability experiment of 2x4 PP Lego™ block	28
Figure 3.12	Font view of gauge block used to measure the repetability of 2x4 Lego™ blocks . . . . .	29
Figure 3.13	Detail of flexures to hold capacitive probes and ejection pins to disassemble the blocks . . . . .	29
Figure 3.14	Lego™ block with aluminum sheet used as a target for the capacitive probes	29
Figure 3.15	Lego™ block position in 30 cycle assembly-disassembly sequence, first bench level experiment . . . . .	31
Figure 3.16	Bottom and top view of the epoxied monolithic block used for the repetability vs. number of contact points bench level experiment . . . . .	32
Figure 3.19	Experimental setup for the second bench level experiment . . . . .	33
Figure 3.17	Second bench level experiment using two 6x2 PP’s blocks (72 contact points) . . . . .	33
Figure 3.18	Second bench level experiment using five 6x2 PP’s blocks (180 contact points) . . . . .	33

Figure 4.1	Structural loop of a milling machine . . . . .	38
Figure 4.2	Structural loop of a mechanical coupling . . . . .	38
Figure 4.3	Identification of Product Values and Goals . . . . .	39
Figure 4.4	Concept Selection Chart . . . . .	40
Figure 4.5	Anisotropic wet etch and mask . . . . .	41
Figure 4.6	Isotropic wet etch and mask . . . . .	41
Figure 4.7	Coupling array distribution on 4 inch wafer, notice the array orientation is in $\langle 110 \rangle$ . . . . .	45
Figure 4.8	Detailed view of the convex coupling array concept, notice the cantilevers and the KOH etched pyramids at the cantilever tips . . . . .	45
Figure 4.9	Detail of concave coupling (V-groove) on boss . . . . .	46
Figure 4.10	Detail of coupling pair . . . . .	46
Figure 4.11	Silicon “pit” etched through wet anisotropic etch, using a concave cornered mask . . . . .	47
Figure 4.12	Detail of CCS, after Zhang [25] . . . . .	48
Figure 4.13	Mask used to etch the pyramids . . . . .	48
Figure 4.14	Detailed view of Mask M-1 with overlapped Masks M-2 and F-1 . . . . .	50
Figure 4.15	Detailed view of Mask M-2 with overlapped Masks M-1 and F-1 . . . . .	50
Figure 4.16	Detail of Mask F-1 with overlapped Masks M-1 and M-2 . . . . .	50
Figure 5.1	Pyramid masked with stoichiometric silicon-nitride, the thin film residual stress caused jagged edges and rough surface finish . . . . .	53
Figure 5.2	Detail of stoichiometric silicon-nitride masked pyramid, showing jagged edges and rough surface finish . . . . .	53
Figure 5.3	Pyramid masked with CVD silicon-nitride, shown after nitride strip. The low residual stress film yields sharp edges and smooth sidewalls after the KOH etch . . . . .	54
Figure 5.4	Detail of CVD silicon-nitride masked pyramid after KOH etch. Picture taken after nitride strip. . . . .	54
Figure 5.5	Front view SEM image of the convex coupling feature, (wafer 1). Traces of the convex corner compensating structures can be seen on the lower corners of the pyramid . . . . .	55
Figure 5.6	SEM side view image of the convex coupling feature array, (wafer 1) . . . . .	55
Figure 5.7	Front view SEM image of the convex coupling feature after release (wafer 2) . . . . .	55
Figure 5.8	SEM side view image of the convex coupling feature array (wafer 2) . . . . .	55

Figure 5.9	SEM picture of concave feature boss and V-groove . . . . .	56
Figure 5.10	Detail of boss and V-groove, showing rough surface finish on the boss and V-groove side-walls . . . . .	56
Figure 5.11	Dimensions of the CCCS, after Zhang [25] . . . . .	57
Figure 5.12	CCCS dimensions for pyramid masking . . . . .	59
Figure 5.13	CCCS experiment mask . . . . .	59
Figure 6.1	Measurement set-up used to test the passive wafer alignment features. Electronics Vision TBM8 . . . . .	64
Figure 6.2	Wafer chuck and top CCD objective. The measurement coordinate system is indicated . . . . .	64
Figure 6.3	Detailed view of passive wafer aligned stack. Note the cantilevers and bottom wafer showing on the left side of the stack . . . . .	64
Figure 6.4	Detail of V-groove damage after M-1 & F1 wafer testing . . . . .	68
Figure 6.5	Detailed of V-groove damage after M-1 F-1 wafer testing. The shadowed area is the tapered sidewall of the V-groove . . . . .	68
Figure B.1	Mask M-1 . . . . .	82
Figure B.2	Mask M-2 . . . . .	83
Figure B.3	Mask F . . . . .	84
Figure C.1	CCCS optimization, die E1 . . . . .	85
Figure C.2	CCCS optimization, die E2 . . . . .	85
Figure C.3	CCCS optimization, die E3 . . . . .	86
Figure C.4	CCCS optimization, die G1 . . . . .	86
Figure C.5	CCCS optimization, corner detail die G1 . . . . .	86
Figure C.6	CCCS optimization, die G2 . . . . .	86
Figure C.7	CCCS optimization, die G3 . . . . .	87
Figure C.8	CCCS optimization I1 . . . . .	87
Figure C.9	CCCS optimization, die I2 . . . . .	87
Figure C.10	CCCS optimization, die I3 . . . . .	87



# LIST OF TABLES

TABLE 3.1	Repeatability of 2x4 PP Lego™ block . . . . .	30
TABLE 3.2	“Cap” test for second bench level experiment . . . . .	34
TABLE 3.3	Repeatability results of second bench level experiment . . . . .	35
TABLE 4.1	CCCS dimensions for different etch depths . . . . .	48
TABLE 4.2	Concave and concave feature size targets . . . . .	49
TABLE 5.1	CCCS dimensions for various etch depths, applying equation 5.1 . . . . .	58
TABLE 5.2	CCCS sizing experiment combinations . . . . .	59
TABLE 5.3	CCCS sizing experiment results . . . . .	60
TABLE 6.1	Cap test results, wafers M-1 & F-1, preloaded . . . . .	65
TABLE 6.2	Test results Wafers M-2 & F-1, all cantilevers . . . . .	66
TABLE 6.3	Test results wafers M-1 & F-1, no preload besides top wafer mass . . . . .	67
TABLE 6.4	Test results wafers M-2 & F-2, no preload besides top wafer mass . . . . .	69
TABLE A.1	Concave coupling process . . . . .	78
TABLE A.2	Convex coupling process . . . . .	79
TABLE D.1	Cap Test data, wafers M-1 & F-1 preloaded . . . . .	90
TABLE D.2	Test data Wafers M-2 & F-1, all cantilevers . . . . .	91
TABLE D.3	Test data wafers M-1 & F-1, no preload besides top wafer mass, 96 cantilevers . . . . .	92
TABLE D.4	Test data wafers M-1 & F-1, no preload besides top wafer mass, 88 cantilevers . . . . .	92
TABLE D.5	Test data wafers M-1 & F-1, no preload besides top wafer mass, 80 cantilevers . . . . .	93
TABLE D.6	Test data wafers M-1 & F-1, no preload besides top wafer mass, 72 cantilevers . . . . .	93
TABLE D.7	Test data wafers M-1 & F-1, no preload besides top wafer mass, 64 cantilevers . . . . .	94
TABLE D.8	Test data wafers M-1 & F-1, no preload besides top wafer mass, 56 cantilevers . . . . .	94
TABLE D.9	Test data wafers M-1 & F-1, no preload besides top wafer mass, 48 cantilevers . . . . .	95

TABLE D.10 Test data wafers M-2 & F-2. no preload besides wafer mass, 96 cantilevers . . . . .	95
TABLE D.11 Test data wafers M-2 & F-2. no preload besides wafer mass, 88 cantilevers . . . . .	96
TABLE D.12 Test data wafers M-2 & F-2. no preload besides wafer mass, 80 cantilevers . . . . .	96
TABLE D.13 Test data wafers M-2 & F-2. no preload besides wafer mass, 72 cantilevers . . . . .	97
TABLE D.14 Test data wafers M-2 & F-2. no preload besides wafer mass, 64 cantilevers . . . . .	97
TABLE D.15 Test data wafers M-2 & F-2. no preload besides wafer mass, 56 cantilevers . . . . .	98
TABLE D.16 Test data wafers M-2 & F-2. no preload besides wafer mass, 48 cantilevers . . . . .	98
TABLE D.17 Test data wafers M-2 & F-2. no preload besides wafer mass, 40 cantilevers . . . . .	99
TABLE D.18 Test data wafers M-2 & F-2. no preload besides wafer mass, 32 cantilevers . . . . .	99
TABLE D.19 Test data wafers M-2 & F-2. no preload besides wafer mass, 24 cantilevers . . . . .	100
TABLE D.20 Test data wafers M-2 & F-2. no preload besides wafer mass, 16 cantilevers . . . . .	100
TABLE D.21 Test data wafers M-2 & F-2. no preload besides wafer mass, 8 cantilevers . . . . .	101

# Chapter 1

## INTRODUCTION

### 1.1 Background

The objective of this thesis is to review the current commercial wafer alignment technology, investigate common precision alignment principles used in the macro-scale, and to develop, based on fundamental principles, an alternative approach to wafer alignment using the principles of elastic averaging and exact constraint design. The manufacturing process used to create the alignment devices and the results obtained through testing are then presented.

Wafer bonding is a key process in the semiconductor industry. It is used extensively for the fabrication of Micro-Electro-Mechanical-Systems (MEMS) and in the microelectronics industry. Two major applications of wafer bonding in the MEMS field are fabrication and packaging. In the microelectronics industry, wafer bonding is used for CMOS chip scale packaging and 3-D chip and wafer level interconnects.

Wafer bonding enables the fabrication of complex MEMS devices by stacking and bonding individually processed wafers to create complete assemblies. Even if it is possible to make the complete device on a single wafer, the design is often partitioned and wafer bonding is used to simplify the fabrication process of the whole device.

Some MEMS devices, such as accelerometers and gyroscopes are vacuum packaged to protect the moving parts, reduce damping, and to prevent contamination. A significant part of the cost of any MEMS device is attributed to its packaging. On some devices the cost associated with packaging can be higher than the device itself [1]. Wafer bonding can provide chip scale packaging of MEMS and integrated circuits (IC's). Certain types of bonds performed under vacuum can replace expensive ceramic packages [2].

3-D interconnection of IC's consists of face-to-face and face-to-back bonded die stacks. The wiring is achieved through high aspect ratio vias, such as plug and bridge types, which significantly reduces the size of the electrical connections from the order of centimeters to the order of micrometers. Unlike monolithic devices, 3-D interconnected IC's can be packaged much smaller than monolithic devices, and offer the potential of reducing fabrication and performance limitation of planar IC's [3]. 3-D interconnection can be performed on die, wafer, and hybrid levels.

## **1.2 Motivation**

In most cases, both wafers to be bonded have features patterned or deposited on them; thus alignment of the wafers to each other is critical during the bonding step. The overall size and performance of the bonded device, MEMS, chip-scale-packaged IC or 3-D interconnected IC, strongly depends on the alignment accuracy that can be achieved during the bonding step. Die shrink and complex multi-wafer devices are constrained by the alignment capability of the bonding process. This trend has made precision wafer alignment a "bottleneck" that hinders significant development in both the MEMS and microelectronics fields. The current wafer alignment technology, available through standard commercial equipment, must be evaluated in order to propose alternative solutions that could yield better alignment capability.



# Chapter 2

## CURRENT WAFER AND MEMS ALIGNMENT PRINCIPLES

### 2.1 Wafer alignment through optical systems

Wafer to wafer alignment is done using actuation stages and optical systems. All major alignment techniques, such as, infrared alignment, through-wafer via holes, transparent substrate alignment, wafer backside alignment, and inter-substrate alignment, follow the same sequence. Optical systems are used to locate the position of two wafers relative to each other by viewing alignment marks. Once the alignment features on both wafers have been found, a stage varies  $x$ ,  $y$  and  $\theta_z$  of the unconstrained wafer to overlap the alignment features of the fully constrained wafer. The stage then lowers the wafers (varying  $z$ ) onto each other until the wafer's surfaces mate. At this point, the wafers can be bonded.

The alignment capability of these processes can be evaluated analytically by performing an error budget analysis. The alignment error of these systems can be attributed to five main sources: the alignment features themselves, a metrology error partly due to diffraction effects, an actuation error, an error introduced by the mechanism that brings the two wafers in contact ( $z$  translation), and various other errors dependent on wafer material and bonding process, such as the deformation of the wafers once they have been pre loaded, thermal errors, etc.

Alignment features are etched or deposited on the wafer. Etching and deposition are time dependent processes, subject to minimal, but significant size variations. Through wafer

via hole alignment is more subject to this source of error as a high aspect ratio feature is etched through the whole wafer. In the case of wafer backside alignment, an additional source of error is introduced through patterning of the alignment marks on the back of the wafer.

The metrology error is process and wafer dependent. In the case of infrared alignment, the transparency of the silicon is dependent on the doping concentration and surface roughness of the wafer. Double-sided polished wafers are needed to “view” through both wafers.

The actuation stage introduces a random error due to the limited resolution of the  $x$ ,  $y$ ,  $\theta_z$  encoded actuators and systematic errors.

The systematic stage error is strongly dependent on the length of the structural loop. In the case of infrared alignment, through-wafer via holes and back-side alignment, the travel is less than 50  $\mu\text{m}$ , whereas, in the case of inter substrate alignment, the travel can be in excess of 60 mm. Choosing the smallest structural loop possible minimizes this error.

Error due to substrate deformation, thermal error, and error due to material property mismatch is not included in the error budget of the aligner. These errors are bonding process and wafer material dependent and should be dealt with separately for each individual bonding application.

The literature reports that sub-micron level alignment accuracy cannot be achieved with these systems [4].

## **2.2 Passive alignment in Optical MEMS**

The principle of passive alignment has a huge application in the MEMS field and has been extensively applied to optical fiber alignment [5,6,7]. Optical fibers are preloaded against V-grooves by a surface micromachined flexure. The v-grooves are bulk micromachined in silicon using wet anisotropic etchants, such as, highly concentrated potassium hydroxide

(KOH), tetramethylammoniumhydroxide (TMAH), and ethylenediaminepyrocatechol (EDP) solutions. These bases etch the silicon at different rates, depending on the crystalline orientation, and thus expose the slower etching planes, such as (111). In the case of (100) oriented silicon, the (111) planes are at  $54.7^\circ$  from the wafer surface.

It is interesting to note that in spite of the abundance of literature describing similar passive means of alignment for optical fibers, this principle has not been applied for wafer-to-wafer alignment.



# Chapter 3

## MACRO-SCALE PRECISION ALIGNMENT

### 3.1 Precision Machine Design Alignment Principles

Whenever two solid bodies are positioned with respect to each other, the quality of the alignment can be described in terms of the following two parameters: repeatability and accuracy. Repeatability is defined as the degree to which a part will vary its original position over time as it is being assembled and disassembled continuously. Accuracy is defined as the degree to which the part's position matches the desired position. Accuracy can only be achieved if the system's repeatability is good enough; however good repeatability does not ensure acceptable accuracy. Once the system's repeatability is acceptable, accuracy can be improved through adjustment and calibration.

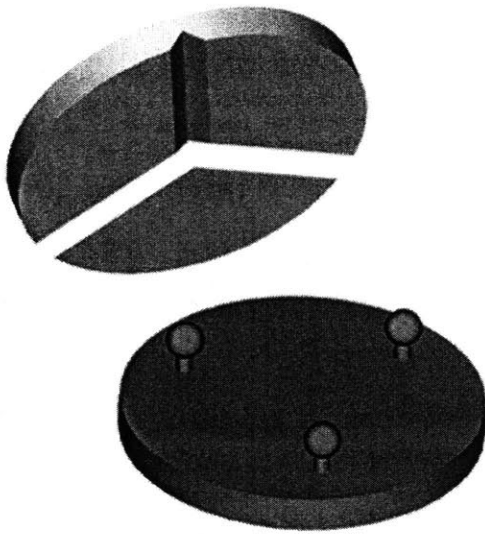
Two basic principles, kinematic design and design for elastic averaging, are capable of providing high repeatability in the location of solid bodies to each other, beyond that obtainable by simple pins and slots [8]. These principles are used extensively by precision machine designers for the design of macro-scale systems. They may have an important application in wafer-to-wafer alignment of micro-scale systems, particularly in the MEMS and microelectronics fields.

### 3.1.1 Kinematic Couplings

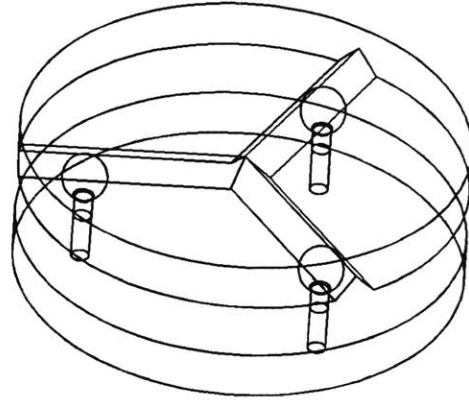
Kinematic couplings are deterministically designed, static, structural couplings. In a deterministic system, the number of contact points between two solid models matches the number of degrees of freedom which are restricted. As the body is exactly constrained, its position can be determined in a closed form solution [8]. However, the point loads required by a deterministic system may cause significant Hertzian contact stress on the couplings which limits its application. Repeatability of  $0.1\mu\text{m}$  has been reported with the use of heavily loaded steel ball and groove couplings. This material is subject to fretting corrosion, which requires wear-in and degrades the repeatability for high-cycle applications. Ceramic kinematic couplings are not subject to fretting corrosion and can be used with little or no wear-in [9]. The repeatability of a well-designed and preloaded ball and groove kinematic coupling is in the order of the surface finish of the grooves. Due to the low number of supports and high contact stresses, the stiffness of kinematic couplings is low compared to a surface-to-surface joint.

Kinematic couplings make use of concave features that fit into grooves. The shape of the grooves depend on the number of contact points that are required between the groove and the convex feature. If six degrees of freedom are constrained, one can choose to constrain three convex features in two degrees of freedom (DOF) each, as is the case with a three-groove kinematic coupling. Alternatively, one convex feature can be constrained in three DOF (i.e in a trihedral socket), a second convex feature in two DOF (using a regular V groove) and the last convex feature in one DOF (i.e a flat surface). Figures 3.1 and 3.2 show a three-groove kinematic coupling.

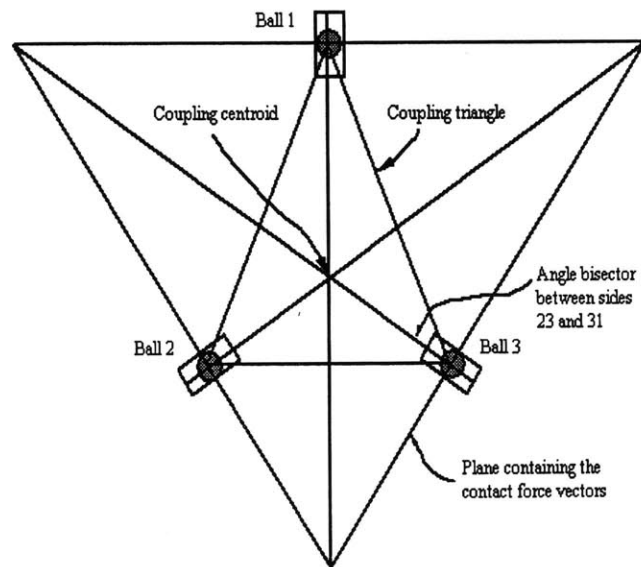
To ensure stability in a three-groove kinematic coupling, the grooves must be arranged in a triangular fashion, such that the normals to the planes created by the two contact points of each coupling, intersect within the coupling triangle [9] as shown in Figure 3.3.



**Figure 3.1** Three-groove kinematic coupling disassembled



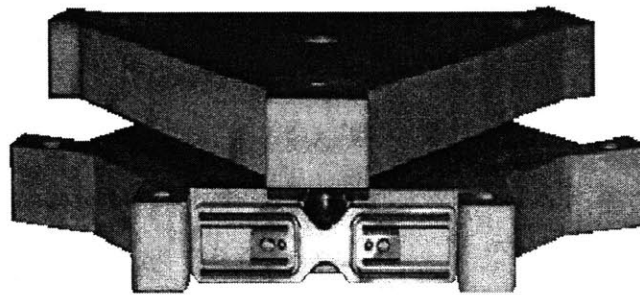
**Figure 3.2** Three-groove kinematic coupling assembled



**Figure 3.3** Coupling arrangement to ensure stability (figure by A. H. Slocum, *Design of three-groove kinematic couplings* [9])

### 3.1.2 Flexural Kinematic Couplings

Kinematic couplings can provide very high repeatability. The price paid is a low joint stiffness, when compared to a surface-to-surface joint, and the fact that the surfaces of the joined parts don't mate. This is a drawback if the two parts to be joined are intended to seal. One way of increasing the joint stiffness and to allow the joined parts to mate while still achieving high repeatability, is to mount the kinematic coupling elements, either the concave features or the v-grooves, on flexures, such that, when the coupling is lightly preloaded, it works as a regular kinematic coupling. As the preload is increased, the flexures bend until the surfaces of both bodies come into contact. The kinematic coupling is then fully pre-loaded and the rest of the load is taken by the mating surfaces. Although the repeatability is slightly lower than the one in regular kinematic couplings, the joint's stiffness is increased significantly. This is the idea behind the "Kinflex" design, shown in Figure 3.4. [10].



**Figure 3.4** Flexural kinematic coupling "Kinflex" (US patent 5,678,944 [10])

### 3.1.3 Elastic Averaging

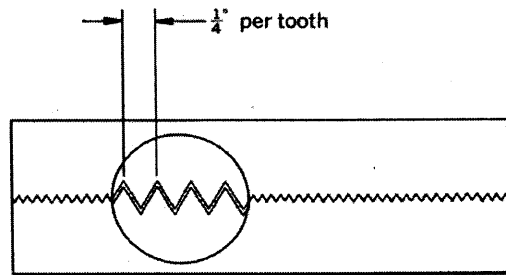
Contrary to kinematic design, elastic averaging is based on significantly over-constraining the solid bodies with a large number of relatively compliant members. As the system is preloaded, the elastic properties of the material allow for the size and position error of each individual contact feature to be averaged out over the sum of contact features throughout the solid body. Although the repeatability and accuracy obtained through elas-



tic averaging may not be as high as in deterministic systems, elastic averaging design allows for higher stiffness and lower local stress when compared to kinematic couplings.

In a well designed and preloaded elastic averaging coupling, the repeatability is approximately inversely proportional to the square root of the number of contact points [11].

Hirth or curvic couplings, used in serrated tooth circle dividers, shown in Figure 3.5, are examples of elastically averaged couplings. The serrated tooth circle divider uses two mating face gears. Both are the same diameter and have equal tooth geometry and tooth size. As the two face gears are engaged and preloaded, the teeth are lapped, the individual tooth size and position variations are averaged out over all the teeth, thus providing good repeatability [12].

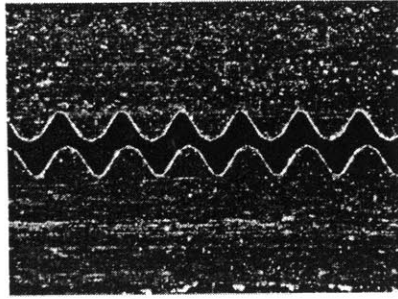


**Figure 3.5** Circle divider (figure by W. R. Moore, *Foundations of mechanical accuracy* [12])

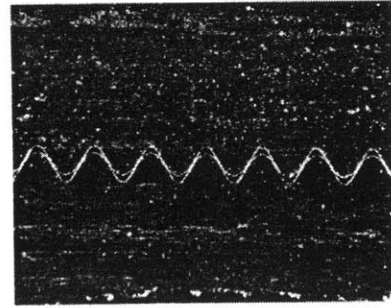
Figure 3.6 shows a detailed view of the face gears disengaged. Figure 3.7 shows the same face gears engaged.

This type of coupling relies on stiff elements and requires large preloads. Furthermore these type of couplings often require a wear-in period to achieve very high repeatability.

The principle of elastic averaging can also be applied to designs that use more compliant members, thus requiring a smaller preload. An example of an elastic averaged coupling based on low stiffness elements are Lego <sup>TM</sup> blocks.



**Figure 3.6** Curvic coupling disengaged (figure by W. R. Moore, *Foundations of mechanical accuracy*[12])



**Figure 3.7** Curvic coupling engaged (figure by W. R. Moore, *Foundations of mechanical accuracy*[12])

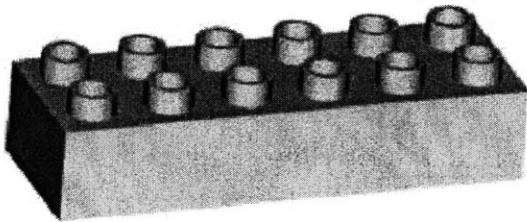
### 3.2 Elastic Averaging Bench Level Experiment

Elastic averaging can be used to accurately locate solid bodies, and may potentially play an important role in locating MEMS structures in a die or with respect to another MEMS device. To investigate this potential, a series of experiments were performed on Lego™ Duplo™ blocks to qualitatively evaluate the repeatability that can be obtained through this principle. The press-fit assembly design of Lego™ blocks makes use of the elastic averaging principle, obtaining high repeatability [13,14].

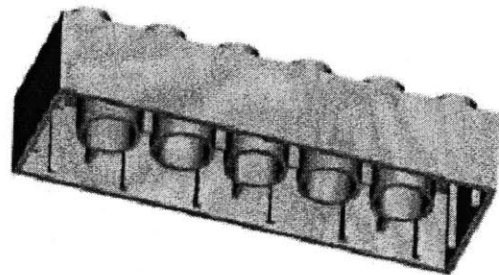
Tests showed that the particular toy blocks used in the experiment, when assembled and preloaded effectively, have a repeatability of less than 5  $\mu\text{m}$ . It is anticipated that the actual repeatability can be improved from the one reported by better controlling the pre-load; nevertheless, the repeatability we measured is still quite impressive.

Lego™ blocks are prismatic, thin-walled, plastic toy blocks provided with projection or bosses symmetrically distributed on the top and bottom faces of the blocks [13]. Figures 3.8 and 3.9 show the top and bottom view of a 2x6 primary projection (PP's) building block. Primary and secondary projections are arranged such that, when the blocks are placed on top of each other, the primary projections of the bottom block engage with the secondary projections of the top block. Each projection engages in exactly three contact

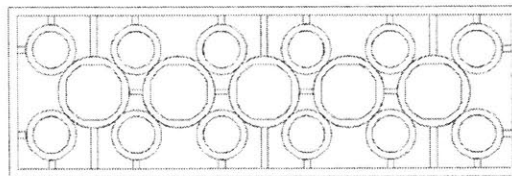
lines with its mating geometry [14], as shown in Figure 3.10. The dimension and location of the projections allows for the blocks to be press fitted on to each other [13]. The slight interference fit between the engaged projections of different blocks creates the necessary frictional engagement, or holding force, to keep both blocks fixed to each other [13].



**Figure 3.8** Top view of 2x6 PP building block



**Figure 3.9** Bottom view of a 2x6 PP building block



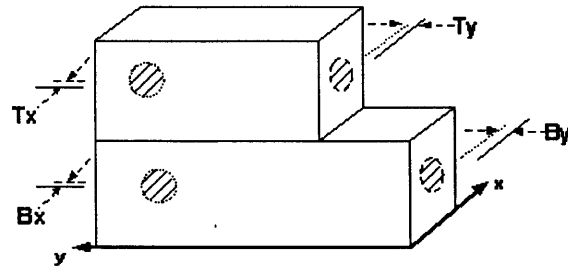
**Figure 3.10** Cross-section at the interface of two blocks showing three line contact of every primary projection with adjacent secondary projections

### 3.2.1 Repeatability of a 2X4 Projection Lego™ block

A series of experiments was performed on Lego™ Duplo™ blocks to determine the repeatability that can be obtained through elastic averaging on ABS injection molded parts.

The experiment consisted of repeated assembly and disassembly of A and B type blocks. Type A (96mm x 32mm x 19mm in size) and Type B (about 64mm x 32mm x 19mm in

size). Type A block has 12 primary and 5 secondary projections. The shorter block (Type B) has 8 primary and 3 secondary projections. The position (sides and top face) of each block was recorded through every cycle, as shown in Figure 3.11.



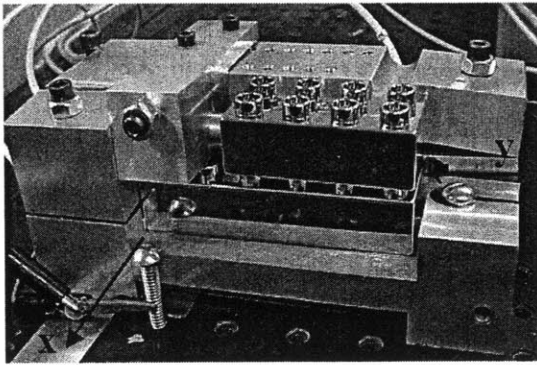
**Figure 3.11** Measurement target for repeatability experiment of 2x4 PP Lego™ block

In a first set-up, the data was taken with a CMM. The same experiment was repeated using capacitive probes. Capacitive sensing was preferred because of its high resolution, repeatability, and accuracy (linearity) [15]. The resolution of the measurement system use in this bench level experiment is  $5 \mu\text{m}$  for the CMM and  $0.05 \mu\text{m}$  for the capacitive probes.

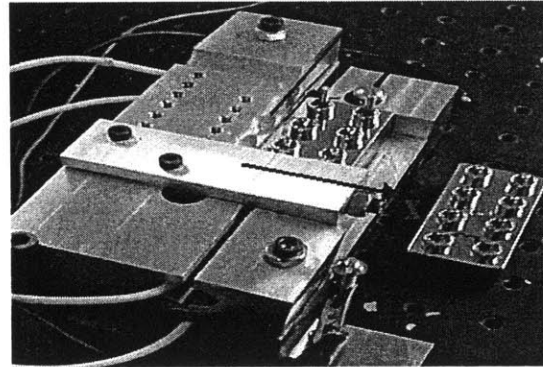
A gauge block, shown in Figures 3.12 and 3.13, was designed to mount the capacitive probes and constrain the bottom Lego™ block. The main requirements of the gauge block were high precision and low distortion. The design was chosen to provide a tight structural loop. Making the complete block one solid piece and directly probing the Lego™ block faces, minimized the Abbe error. The block consists of a central pocket to which the bottom building block has been epoxied. Capacitive probes are mounted on flexures on two faces orthogonal to each other.

Ejection pins were used to disassemble and assemble the blocks in order to avoid contacting the capacitive probe during assembly and disassembly. This set-up was needed because of the limited measuring range and the reduced clearance between the blocks and the capacitive probes. Four 3 mm bores were placed into the bottom block to give clear-

ance to the ejection pins. Although the bores slightly reduce the bottom block's stiffness, it is assumed that it does not have a significant effect on the overall repeatability results.

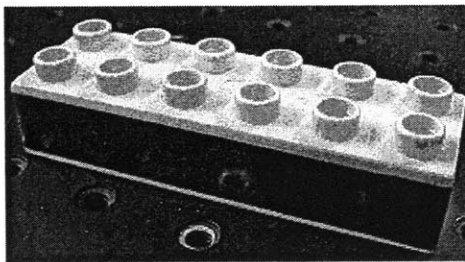


**Figure 3.12** Front view of gauge block used to measure the repeatability of 2x4 Lego™ blocks



**Figure 3.13** Detail of flexures to hold capacitive probes and ejection pins to disassemble the blocks

Capacitive sensing needs a conductive surface as a target, so a 25  $\mu\text{m}$  thick aluminum sheet was glued to each block as shown in Figure 3.14.



**Figure 3.14** Lego™ block with aluminum sheet used as a target for the capacitive probes

The same experiment was repeated using chrome plated Lego™ blocks to eliminate the error introduced at the shim-block interface.

A routine was used to probe the block's position with the CMM in the first set up. In the second and third set-up, the output signal of the capacitive probes was connected to Lab-view™ software through a data acquisition card and recorded for every assembly-disas-

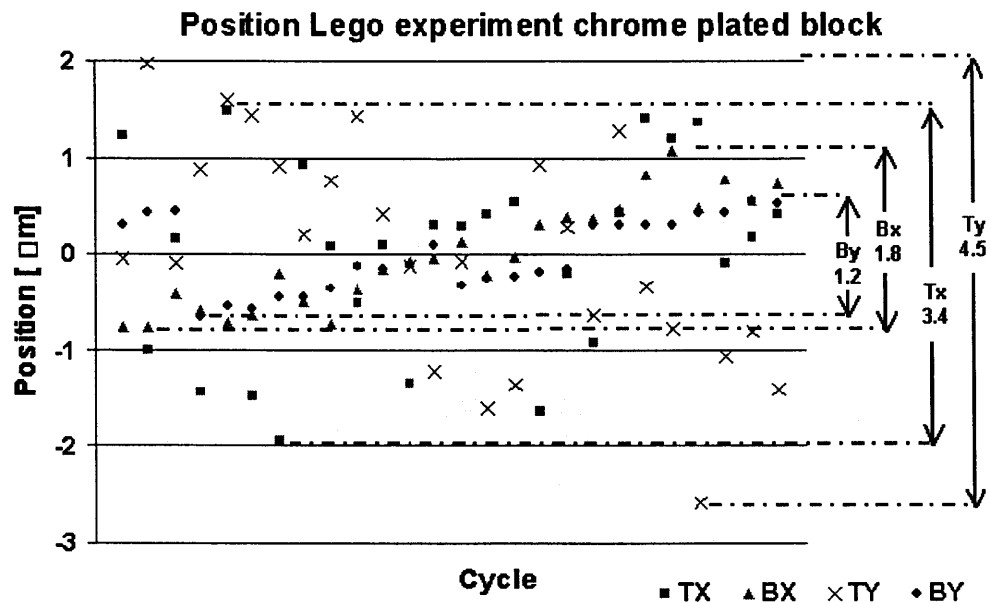
sembly cycle. The block's position was recorded once the readings had stabilized. Creep and thermal stress caused the readings to drift for about two minutes. The output signals were normalized to the first read-out in order to eliminate any signal offset. The outlier measurements (maximum and minimum values) were dropped. The repeatability was calculated as the range of the remaining data<sup>1</sup>. The results of this experiment are presented in Table 3.1.<sup>2,3,4</sup>

**TABLE 3.1** Repeatability of 2x4 PP Lego™ block

Experiment	Bx [ $\mu\text{m}$ ]	Tx [ $\mu\text{m}$ ]	By [ $\mu\text{m}$ ]	Ty [ $\mu\text{m}$ ]	Bz [ $\mu\text{m}$ ]	Tz [ $\mu\text{m}$ ]
CMM	5	19	5	20	5.3	20.3
Capacitive Using bonded sheet target	4.7	14.5	4.5	27.4	N/A	N/A
Capacitive Using chrome plated blocks	1.8	3.4	1.2	4.5	N/A	N/A

A “cap” test with the chrome plated blocks showed that noise in the measurement system accounts for sub-micron ( $10^{-7}\text{m}$ ) error. The cause of non-zero repeatability of the bottom block is attributed to block deformation caused by the assembly and disassembly loads, as well as to thermal induced stress. This was confirmed by seeing a “growing trend” on the read-out of the probes over time, as seen on the plot in Figure 3.15. Some witness marks could be seen in the contact lines of the top block's secondary projections after the experiment had been repeated several dozen load-unload cycles. The data presented was taken from a short, 30 cycle experiment.

1. Some authors define repeatability as half the range. For the results presented herein, repeatability is defined as the range of all data after eliminating outlier values
2. Resolution of the CMM is  $5\mu\text{m}$ , resolution of the capacitive probes is  $0.05\mu\text{m}$
3. Repeatability results taken with CMM after 50 cycles; repeatability results taken with capacitive probes and bonded sheet target after 30 cycles, repeatability taken with capacitive probes on the chrome-plated blocks after 30 cycles
4. Nomenclature after Figure 3.11



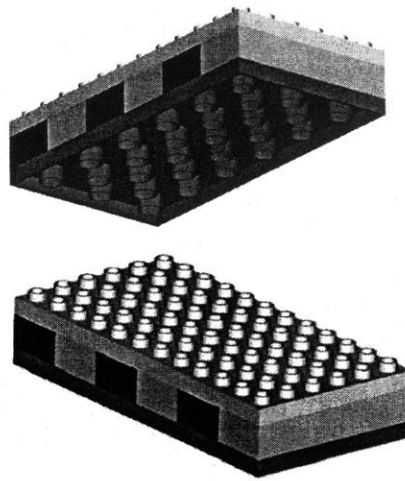
**Figure 3.15** Lego™ block position in 30 cycle assembly-disassembly sequence, first bench level experiment

It was expected that the top blocks repeatability in the y direction ( $T_y$ ) would be better than in the x direction ( $T_x$ ). The top block has 2.5 times more elements in the y direction than in the x direction, and repeatability is inversely proportional to the square root of contact points. This however was not the case, and it is believed that since the assembly force was not carefully controlled during the experiment, the top block did not fully sit on the bottom block during some of the assembly cycles. The block's aspect ratio would cause a larger abbe error in the y direction than in the x direction, causing the unexpected results. In spite of this discrepancy, the repeatability values obtained are quite impressive for these simple toy blocks.

### 3.2.2 Repeatability and number of contact points

A second bench level experiment was designed to evaluate the relationship between the number of contact points and the repeatability of an elastically averaged coupling.

The sequence described in section 3.2.1 was followed, but with a set-up that allowed the number of engaged primary and secondary projections to be varied. Six Lego™ blocks, size 2x6 PP's, were epoxied between two Lego™ plates, size 12x6 PP's, to create a relatively stiff monolithic block with 72 PP's, as shown in Figure 3.16. Two to five 2x6 PP's blocks were placed between two large monolithic blocks as shown in Figures 3.17 and 3.18. This modified the number of contact points between the blocks from 72 to 180.



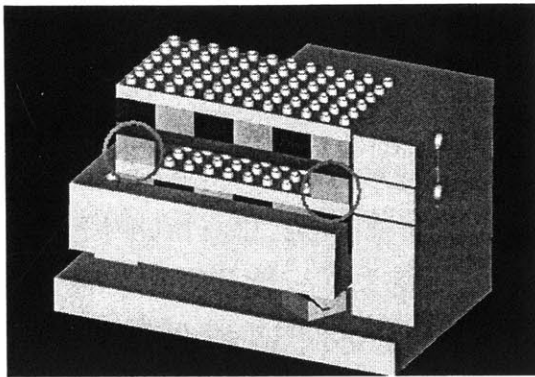
**Figure 3.16** Bottom and top view of the epoxied monolithic block used for the repeatability vs. number of contact points bench level experiment

Three of the 2x6 PP Lego™ blocks, which had previously been chrome plated, were used as targets for the capacitive probes. These target blocks were interconnected through a conductive shim embedded in the epoxied block.

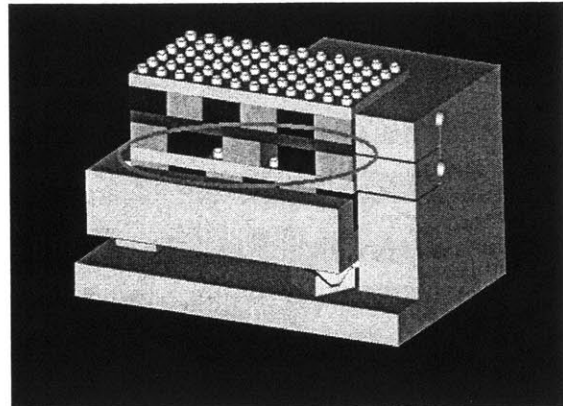
One of the monolithic blocks was epoxied to a moving base, which in turn, was kinematically coupled to the base fixture via three canoe ball type couplings, as shown in Figure 3.19.

The base fixture consists of two main parts: a square block, which serves as a reference plane for X and Y measurements and a base with three press-fitted V-groove inserts, and a



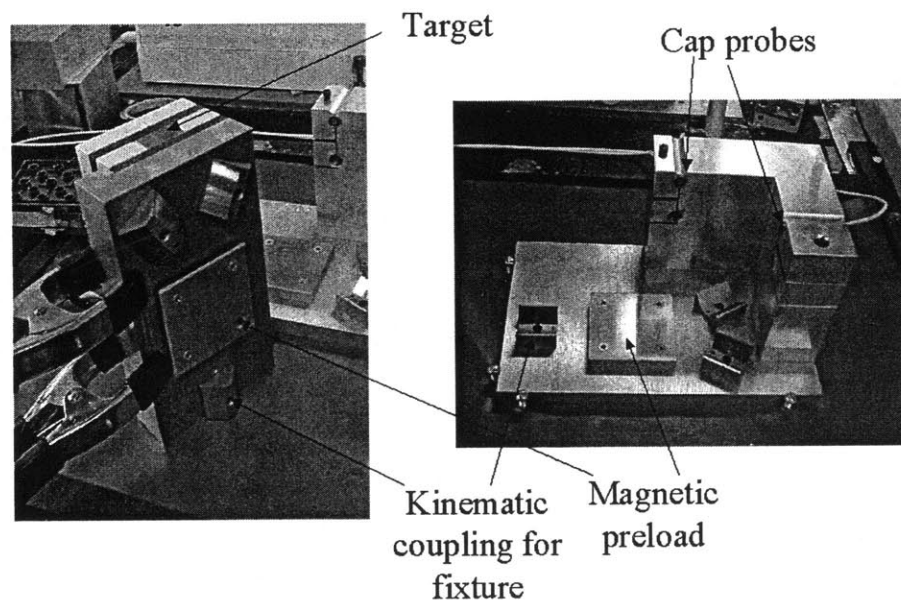


**Figure 3.17** Second bench level experiment using two 6x2 PP's blocks (72 contact points)



**Figure 3.18** Second bench level experiment using five 6x2 PP's blocks (180 contact points)

pocket for a permanent magnet used to increase the kinematic couplings preload. The block constrains four capacitive probes using flexures.



**Figure 3.19** Experimental setup for the second bench level experiment

A two piece, kinematically coupled fixture, as shown in Figure 3.19, is used to allow remote assembly and disassembly the monolithic blocks, without coming in contact with the capacitive probes. The capacitive probes are less than 1 mm away from the chrome

plated Lego™ blocks, and any physical contact with the probe while running the experiment causes drift in the read-out values. The top fixture can be tilted away from the capacitive probes to a safe distance for block assembly and disassembly. The kinematic coupling allows the moving plate to return to the original position relative to the fixture base with very high repeatability. Canoe ball kinematic couplings have been shown to provide sub micron repeatability when subject to heavy pre-loads. The preload for the kinematic couplings in the bench level experiment is provided by the mass of the top fixture and two permanent magnets fixed to the top and bottom fixture. The repeatability of the kinematically coupled setup and the system's noise was determined through a cap test which consisted of repeated assembly and disassembly of the fixtures without disassembling the monolithic blocks. The cap test proved sub-micron repeatability, the results of this test are presented in Table 3.2.

**TABLE 3.2** "Cap" test for second bench level experiment

	<b>Bx</b>	<b>By</b>	<b>Tx</b>	<b>Ty</b>
Repeatability [ $\mu\text{m}$ ]	0.56	0.52	0.23	0.85

Thermal gradients as low as  $0.5^\circ\text{C}$  cause deformations in the aluminum fixture that exceed the repeatability of the blocks. To avoid noise due to this source the whole system was placed in an insulating chamber and the position was recorded after the signal from the capacitive probes had stabilized.

The results of a 25 cycle run with 2,4, and 5 2x3 PP's blocks between the large monolithic blocks are presented in Table 3.3

As expected, both repeatability and standard deviation improve as the number of contact points is increased. Error theory predicts that the repeatability of an elastically averaged coupling is inversely proportional to the number of contact points. Although this is not reflected quantitatively, the experimental results clearly show this trend qualitatively.

**TABLE 3.3** Repeatability results of second bench level experiment

<b>Experiment</b>	<b>X [<math>\mu\text{m}</math>]</b>	<b>Y [<math>\mu\text{m}</math>]</b>	<b>X Stand. dev</b>	<b>Y Stand. dev</b>
2 blocks 72 contact points	8.15	10.95	2.484	2.759
4 blocks 144 contact points	5.47	6.23	1.271	1.737
5 blocks 180 contact points	2.805	3.59	0.768	1.021



# Chapter 4

## DESIGN OF A WAFER-LEVEL PASSIVE ALIGNMENT COUPLING

### 4.1 Product values and goals

Most “active” wafer aligners use stacked precision stages ( $x,y,z,\theta_z$ ) to create a four degree-of-freedom (DOF) mechanism that orients two wafers to each other. This same principle is used in series-type machine tools. Figure 4.1 shows the structural loop of a milling machine.

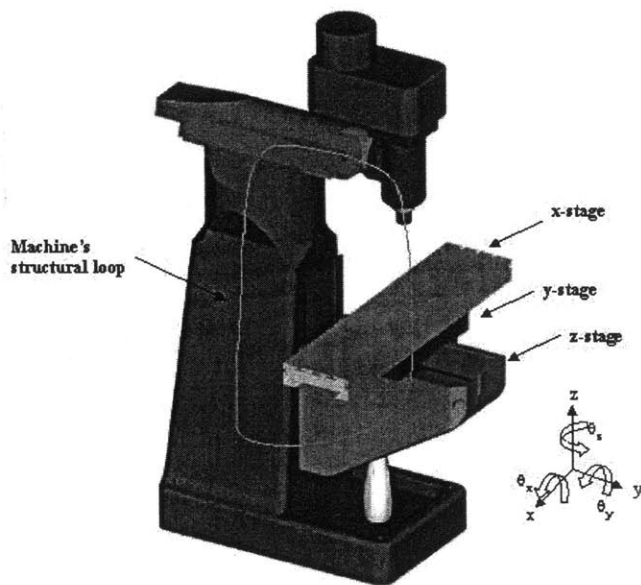
Structural loops are a good indicator of a machine’s stiffness and repeatability. Machines with short and symmetric structural loops are usually stiffer and have better repeatability than machines with large, unsymmetrical machine loops. Mechanical couplings use part-integral features to align two solid bodies to each other. A mechanical coupling creates the shortest possible structural loop between two solid bodies, as shown in Figure 4.2.

An alternative practice for wafer alignment was developed based on the macro-scale principles presented in Chapter 3. Passive wafer alignment is achieved through wafer-integral features, that enable the wafers to “self-align”, when they are stacked onto each other and preloaded.

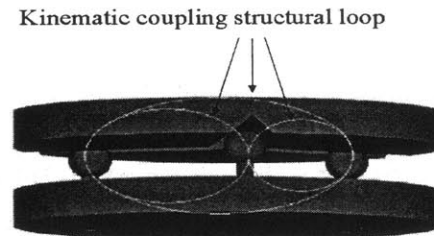
Figure 4.3 shows the incremental identification of product values and goals of a wafer-bonder aligner<sup>1</sup>. This Value Engineering tool aids in identifying the functional require-

---

1. Functional features are squared in, plain text are the designer options or strategies



**Figure 4.1** Structural loop of a milling machine



**Figure 4.2** Structural loop of a mechanical coupling

ments at different levels, generating concepts and focusing the design efforts at the right level [16].

## 4.2 Strategy selection

Applying the principles presented in Chapter 3, several passive alignment design strategies are proposed and evaluated. Figure 4.4 presents a summary of the initial design strategies, including the major risks of each strategy, and a few suggested counter-measures. A detailed analysis of each strategy is presented in Sections 4.2.1 through 4.2.4.

### 4.2.1 Kinematic couplings

Kinematic couplings can achieve the highest repeatability of the alignment principles presented in Chapter 3. Microfabrication of both concave and convex kinematic coupling features is not a trivial task.

High concentration KOH and TaMH solutions are used extensively to etch v-grooves into (100) and (110) silicon. As these bases have crystalline-plane dependent etch-rates, it is

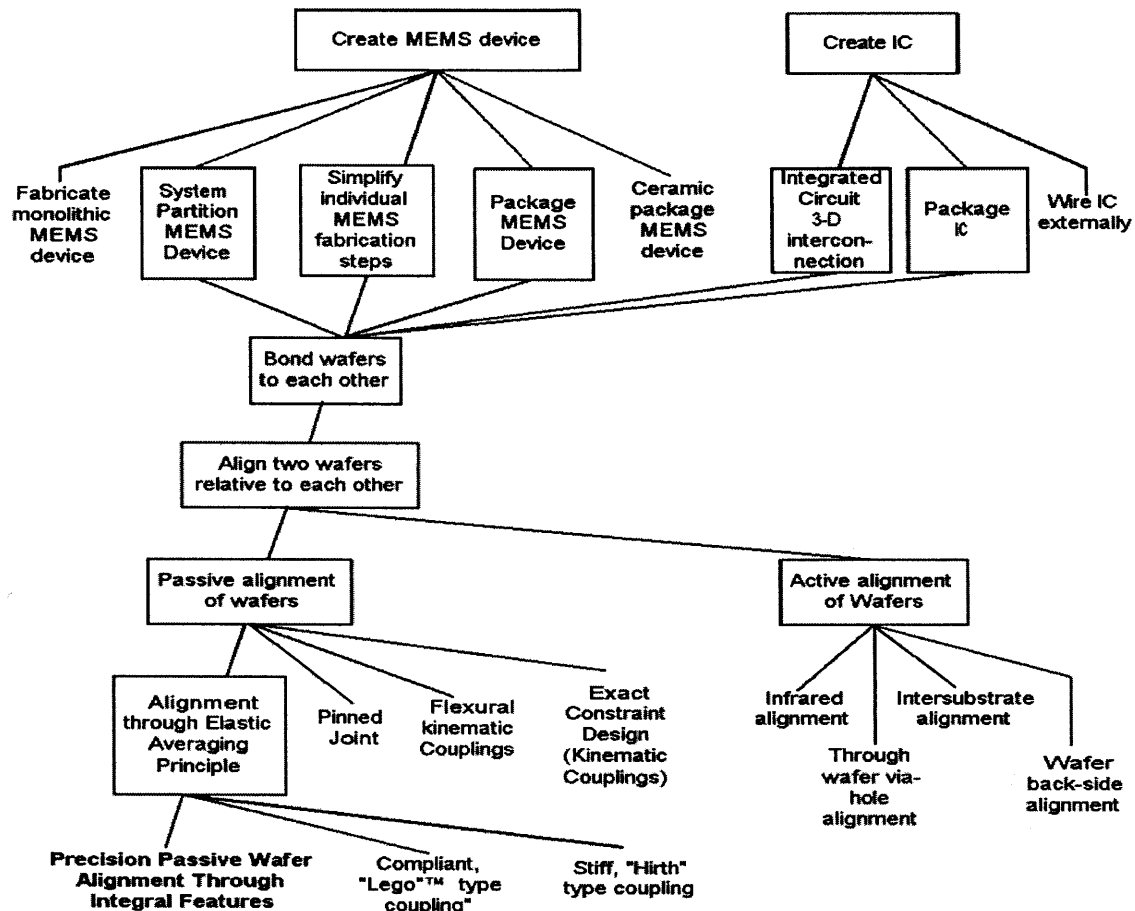


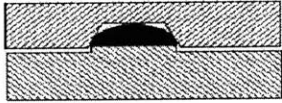
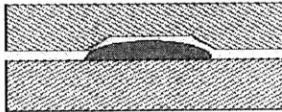
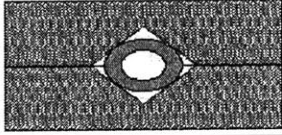

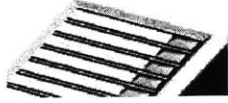
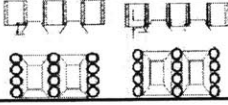
Figure 4.3 Identification of Product Values and Goals

impossible to etch a triangular V-groove arrangement, such as the one shown in Figure 3.3.<sup>1</sup> Circular- and parabolic-sectioned grooves can be fabricated through isotropic etching for any mask orientation. Figures 4.5 and 4.6 show the profiles of anisotropic- and isotropic-etches respectively, and the masks used to create these features.

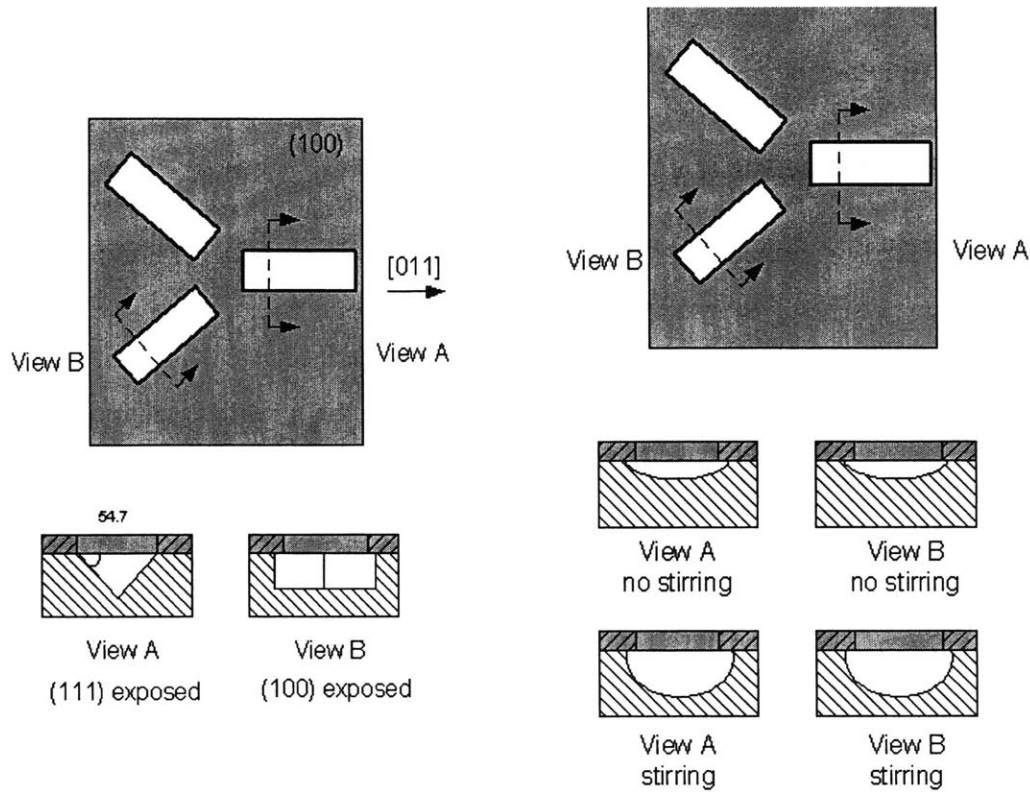
One concept that can be used to create convex flexures or “balls” is to make them out of photoresist using a technique by which spherical convex lenses are made [17]. In this technique, a drop of photoresist is placed on a pedestal. Surface tension and cohesion form a

1. V-grooves of the same geometry can only be wet anisotropically etched perpendicular to each other, regardless of mask orientation or shape. The resulting geometry of a long wet anisotropic etch, obtained from a mask with concave corners, is a rectangular pit inscribing the mask geometry and oriented in  $\langle 110 \rangle$ . For further discussion see Section 4.8.2

Figure 4.4 Concept Selection Chart

Funct. Req.	Design Parameters	Analysis	Ref.	Risks	Countermeasures	Sketch
Kinematic Coupling	Photo resist lens "ball", KOH etched grooves	Process feasibility, Hertz contact stress	[17]	Triangular groove alignment not KOH compatible, organic material not bonding compatible, inherent gap between wafers	DRIE slots + isotropic etch to taper walls, replace PR by non organic material (i.e. silicon or glass spheres)	
Kinematic Coupling	Sputtered Ni mushroom "balls", KOH etched grooves	Process feasibility, Hertz, contact stress	[18]	Triangular groove alignment not KOH compatible, Ni diffusion into Si, delta CTE, inherent gap between wafers	DRIE slots + isotropic etch to taper walls, copper bonding compatible?	
Kinematic Coupling	KOH grooves, optical fiber	Process feasibility, Hertz contact stress calculations	[5] [6] [7]	Triangular groove alignment not KOH compatible, diffusion of Na into Si, delta CTE, inherent gap between wafers, assembly	DRIE slots and isotropic etch to taper walls	
Flexural Kinematic Coupling	Coupling same as KC, add compliance by mounting either "ball" or groove" on flexure	Process feasibility, Hertz contact stress, beam bending	[5] [6] [7] [17] [18]	Same as KC	Same as KC	Same as KC concept sketches, adding flexure on top / bottom wafer
Stiff Elastic Averaging	Etch matching pyramids (islands) and grooves all around wafer OD	Process feasibility, stress calculations, wafer stiffness	-	Wafer deformation / bow	-	
Stiff Elastic Av.	SOI wafer made pins and flexures	Process feasibility	-	Cost	-	-
Compliant Elastic Averaging	Pyramids on grooves, add flexure to pyramid or groove	Process feasibility, beam bending	-	Thinning wafer / boss, process feasibility, wafer bow	Neither too stiff (bow wafer) not too compliant (not align wafer)	
Compliant Elastic Averaging	Pyramids on photo resist (SU8) grooves	Process feasibility, beam bending	-	Organic material, not compatible with bonding	Alternative material	
Pinned Joint	DRIE vias, glass / pin to align wafers	Process feasibility	-	Non sub-micron repeatability	-	-





**Figure 4.5** Anisotropic wet etch and mask

**Figure 4.6** Isotropic wet etch and mask

convex feature which is then hardened by exposing the photoresist to UV light. The tolerances reported however, are not tight enough for a kinematic coupling application; furthermore, wafer bonding is not compatible with any organic material, including photoresist. Isotropic electro-deposition also creates convex structures [18]. However electro-deposited materials (i.e. nickel) have high diffusion rates and are therefore generally not CMOS compatible.

A nearly-kinematic, back-to-back design, can be fabricated by placing an optical fiber between two isotropically-etched wafers. This design requires an assembly step. Sodium diffusion from the optical fiber into the silicon wafer and thermal mismatch are the main risks associated with this strategy.

By far the major disadvantage of applying the principle of kinematic couplings for a wafer bonding application, is the inherent gap that exists between the surfaces of the wafers, as it

prevents the wafers from being bonded; however, this can be overcome by using a flexural kinematic coupling.

### 4.2.2 Flexural kinematic couplings

Flexural kinematic couplings offer good repeatability. When fully preloaded, the surfaces of the two parts being aligned mate. This eliminates the gap present in kinematic couplings. Wafer-level flexural kinematic couplings can be fabricated by using the same techniques proposed for patterning the kinematic couplings on a wafer (section 4.2.1), and mounting either the “ball” or the “groove” on flexures.

The same limitations and process restrictions named for the various kinematic coupling designs apply to the flexural kinematic coupling design.

### 4.2.3 Elastic averaging

Although not as repeatable as kinematic couplings and flexural kinematic couplings, elastic averaging offers acceptable repeatability and the advantage of a high interface stiffness. Additionally, the design can be such, that the parts being aligned mate, which is a key requirement for any bonding process. Three main design strategies for elastically averaged wafer-couplings are evaluated.

The first elastic averaging design strategy is based on the use of stiff features. Arrays of KOH etched pyramids and grooves, placed on the outer diameter of the wafers, can be used to align two wafers back-to-back, just like a Hirth or Curvic coupling. The only difference to a Hirth coupling is that the pyramids and grooves are all oriented along  $\langle 100 \rangle$  and not radially, as is the case in a Hirth / Curvic coupling. The crystalline plane orientation dependent etch-rate was explained in Sections 2.3 and 4.2.1.

The second elastic averaging design strategy is based on compliant features and KOH etched pyramids. High aspect ratio, compliant structures made out of photoresist (SU8) could add the compliance needed to mate the wafer surfaces without causing excessive

deformation on the wafers. This design is not feasible due to the incompatibility of the photoresist with the bonding process.

The third elastic averaging strategy uses KOH etched pyramids and grooves like the stiff elastic averaging design, but adds compliance to the coupling by mounting either the pyramids or the grooves on flexures.

#### **4.2.4 Pinned joints**

This design strategy is based on etching high aspect ratio vias into the wafers and orienting the wafers using silicon or glass pins. Based on macro alignment experience this strategy is not likely to provide sub-micron repeatability.

### **4.3 Design constraints**

As illustrated in Figure 4.3, wafer alignment is a sub-process of wafer bonding. Wafer bonding, in turn, is one out of many processes used to fabricate a complete MEMS / IC device. This process dependence constrains the design of the alignment features and their fabrication process to the following:

- The process used to create the alignment features must be CMOS and microelectronic-process compatible.
- The materials and processes used in fabricating the wafer integral features, must maintain the thermal budget of the device. If for example, a low melting temperature material were to be used for the wafer-integral alignment features, no further processing at temperatures above this threshold could be performed.
- After alignment the wafers must be bondable. Both the alignment principle and the fabrication process of the wafer-integral features must be compatible with wafer bonding processes.

## 4.4 Concept selection

The design constraints stated in section 4.3 rule out the proposed kinematic coupling design concepts, due to the inherent gap between the two wafers being aligned. All designs using organic materials as mechanical elements, i.e. photoresist, are ruled out due to material incompatibility with the bonding process. The use of materials other than silicon is discouraged due to thermal mismatch and risk of diffusion. The silicon on insulator (SOI) design is ruled out because of excessive cost. The stiff-elastic averaging couplings designs are ruled out due to excessive coupling stiffness, which would cause significant wafer strain. Based on process feasibility and the restrictions imposed by the system, elastic averaging using anisotropically etched pyramids and grooves mounted on flexures is selected as the most feasible strategy.

## 4.5 Functional Requirements

Functional requirements are the minimum set of independent requirements that completely characterize the design goals [22]. Unlike constraints, which are a set of non-quantified restrictions, functional requirements are assigned an acceptable tolerance that must be satisfied by the design proposal. The wafer-level passive alignment design functional requirements are:

- Sub-micron repeatability
- Coupling stiffness / wafer stiffness  $\ll 0.01$
- Mating of wafer surfaces after applying preload, eliminating any gaps so the wafers can be bonded

## 4.6 Design parameters

Design parameters are the means by which the functional requirements are fulfilled [23]. Ideally, there is a unique relationship between each one of the design parameters and their

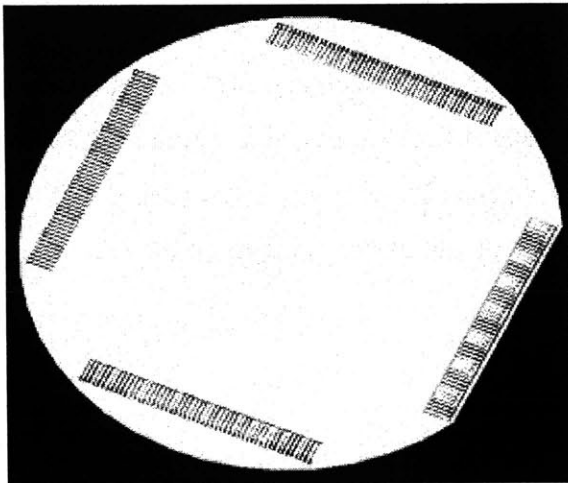
corresponding functional requirement. This way, the design is de-coupled and the individual parameters can be varied arbitrarily to fulfill their corresponding functional requirement without significantly affecting other functional requirements.

In the case of the elastic averaging wafer-alignment design the design parameters are:

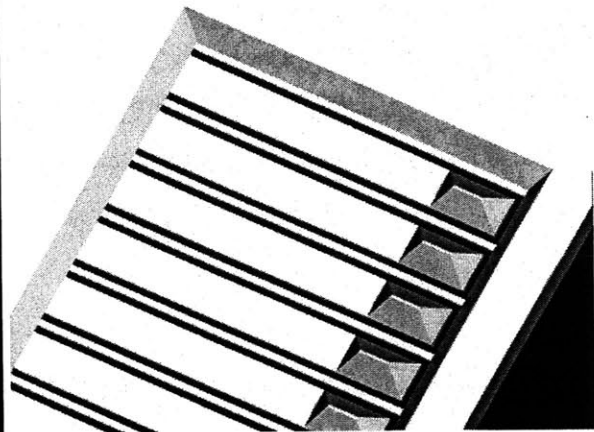
- In plane element stiffness
- Out of plane element stiffness
- Number of contact points

## 4.7 Design layout

The strategy selected relies on anisotropically-etched coupling features mounted on flexures. The coupling features are patterned in arrays orthogonal to each other along the wafer outer diameter, as shown in Figure 4.7. The convex coupling feature, shown in Fig-



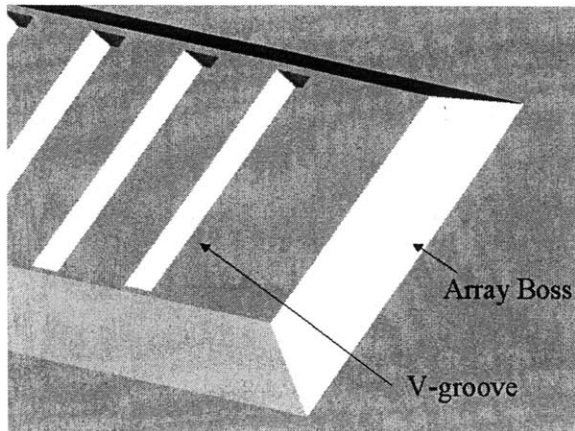
**Figure 4.7** Coupling array distribution on 4 inch wafer, notice the array orientation is in  $\langle 110 \rangle$



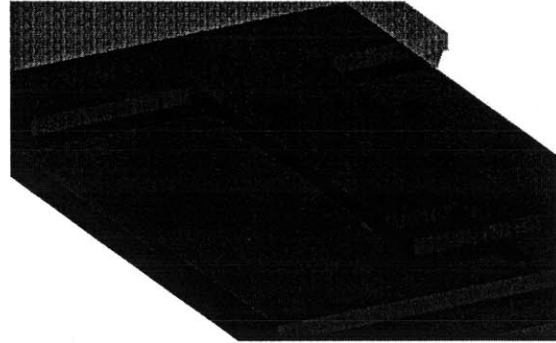
**Figure 4.8** Detailed view of the convex coupling array concept, notice the cantilevers and the KOH etched pyramids at the cantilever tips

ure 4.8, comprises of a KOH etched pyramid mounted on the tip of a silicon cantilever

beam. The concave coupling feature, shown in Figure 4.9 consists of KOH etched V-grooves on a boss. When the wafers are stacked onto each other and preloaded, the pyra-



**Figure 4.9** Detail of concave coupling (V-groove) on boss



**Figure 4.10** Detail of coupling pair

mids at the tip of the cantilevers, slide into the grooves of the convex-coupling features, self-aligning the wafers. The cantilever tips are free to slide along the length of the groove. The only force acting parallel to the cantilever is the friction between the pyramid and the V-groove. Figure 4.10 shows a detailed view of the engagement of one coupling pair. By further preloading wafers, the cantilevers bend until the deflection at the tip is the height of the concave feature boss. The cantilever deflection stops when the surfaces of both wafers have touched. Any additional vertical load on the wafers is taken up by the surface of the wafers.

## 4.8 Manufacturing considerations

The design is constrained by the limitations and requirements of the various process steps needed to make the devices. Sections 4.8.1 through 4.8.5 list the major manufacturing considerations taken.

### 4.8.1 Groove / pyramid layout on wafer

As described in Section 4.2.1, strong bases such as KOH, TaMH and EDP have faster etch rates in certain crystallographic planes than others. In the case of Silicon,  $\{111\}$  planes etch significantly slower than  $\{100\}$  and  $\{110\}$  planes. In the tetrahedral crystalline structure of silicon,  $\{111\}$  planes are orthogonal to each other, so the “pyramids” and “grooves” can only be created normal or parallel to each other. This leads to the array layout shown in Figure 4.7.

### 4.8.2 Principal etch planes of convex-cornered masked features in anisotropic etchants

Long anisotropically-etched features in (100) silicon, made from a concave-cornered mask result in “pits” defined by (111) on the sides, and (100) at the bottom. The pit orientation is in  $\langle 110 \rangle$  direction. The (111) planes frame the mask, regardless of its orientation or shape, as shown in Figure 4.11.

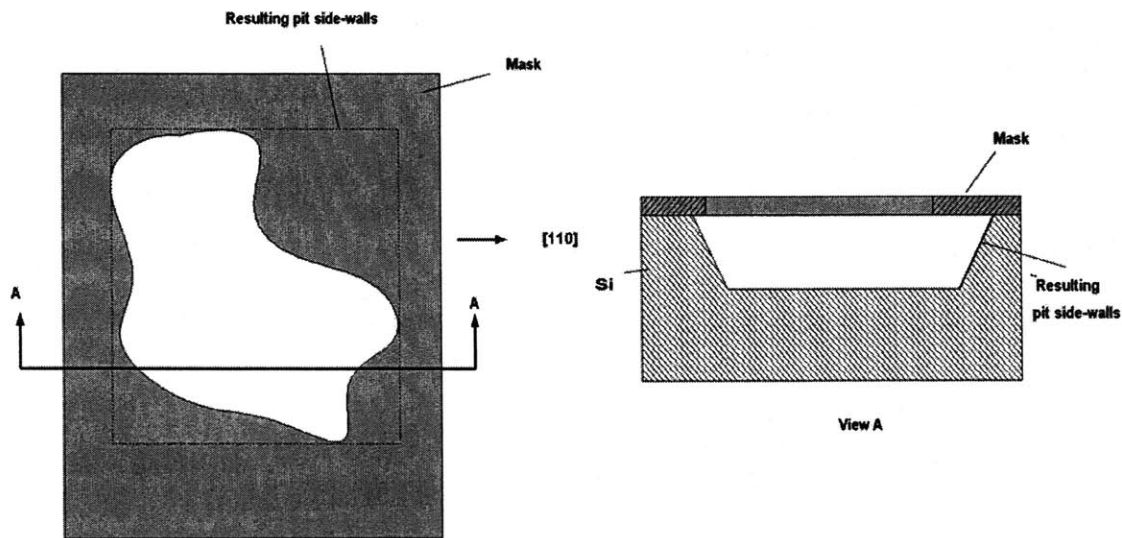


Figure 4.11 Silicon “pit” etched through wet anisotropic etch, using a concave cornered mask

Long anisotropically-etched features in (100) silicon wafers, made from convex-cornered masks, result in “islands” with strong bevelling of the corners due to fast etch rates along

[410] and [411]. For deep etches, corner bevelling, can completely undercut the mask, etching away the “island” structure. Convex corner compensating structures (CCCS) are added to the mask in order to prevent bevelling of the structure’s corners [23]-[25]. Zhang [25] proposes a compact CCCS, shown in Figure 4.12. Applying the CCCS on all four corners of the mask, results in the geometry shown in Figure 4.13.

The size of the CCCS sets the minimum spacing permissible between the convex structures. Table 4.1 shows the mask’s dimensions for different etch-depths. The equations used to calculate the size of the CCCS, as well as additional manufacturing considerations are presented in Section 5.2..

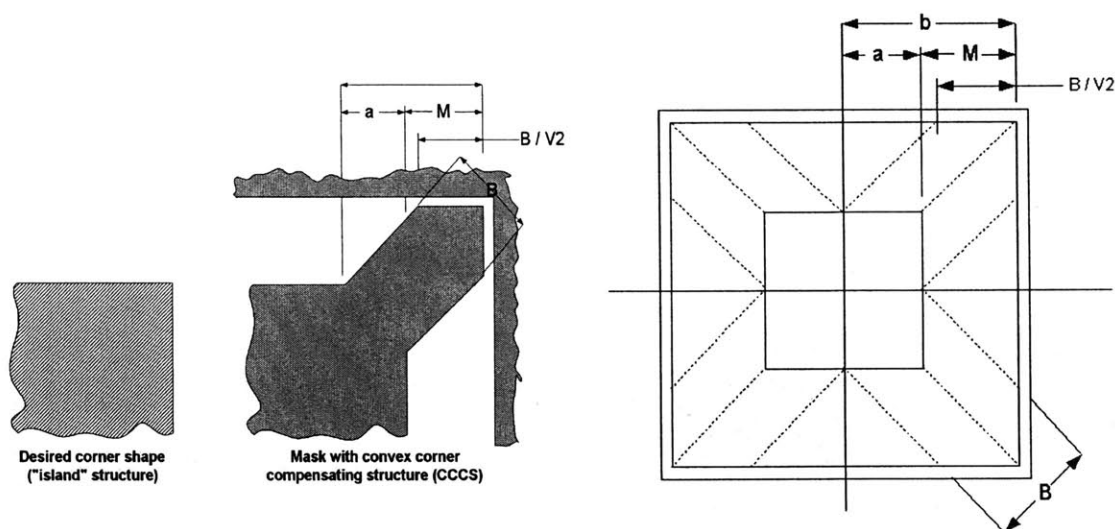


Figure 4.12 Detail of CCS, after Zhang [25]

Figure 4.13 Mask used to etch the pyramids

TABLE 4.1 CCCS dimensions for different etch depths

Etch depth	300 $\mu\text{m}$	350 $\mu\text{m}$	400 $\mu\text{m}$
M [ $\mu\text{m}$ ]	442	512	582
B [ $\mu\text{m}$ ]	758	885	1011
a [ $\mu\text{m}$ ]	536	625	715
b [ $\mu\text{m}$ ]	978	1137	1297



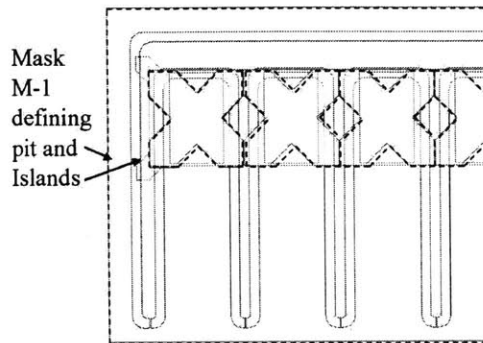
## 4.9 Design detailing

In a first order estimate, the coupling can be modeled using basic beam bending equations. The flexure is modeled as a cantilever beam with an unconstrained end. The cantilevers are designed to have a maximum of 0.2% strain, when bent out of the wafer plane, with a cantilever tip deflection of 150  $\mu\text{m}$ . This low strain value is chosen to prevent material failure due to stress concentration at the  $\{111\}$ - $\{100\}$  interfaces, and to keep the wafer distortion at a low level.

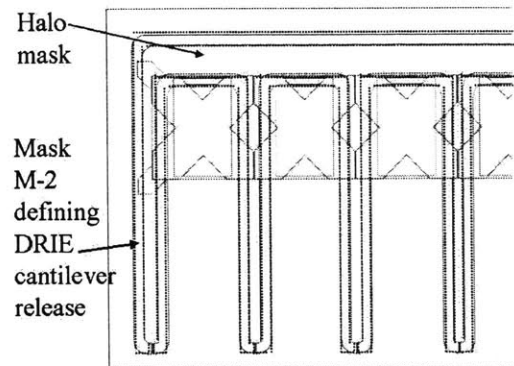
Table 5.4 summarizes the critical cantilever and v-groove dimensions chosen to fulfill the various functional requirements and restrictions. Figures 5.14 through 5.16 show a detailed view of the arrays for masks M-1, M-2 and F-1 respectively. As a reference, the other masks are shown in the background on each figure as well. Figures B-1 through B-3, in Appendix B, show a full view of masks M-1 through F-1.

**TABLE 4.2** Concave and concave feature size targets

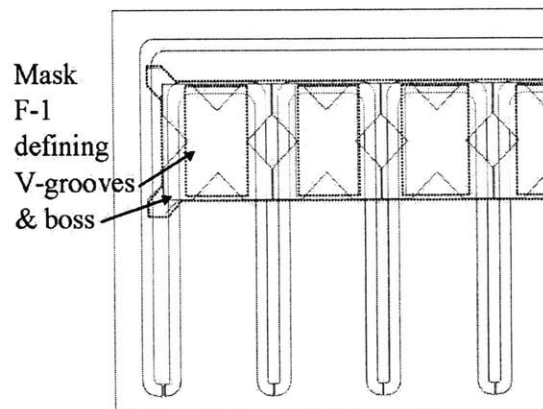
<b>Feature</b>	<b>Mask</b>	<b>Size [<math>\mu\text{m}</math>]</b>
Pit length	Mask M-1	7000
Pit width	Mask M-1	26000
Pit distance from wafer center line (inner edge)	Mask M-1	7500
Cantilever length	Mask M-1 and Mask M-2	5260
Cantilever width	Mask M-2	1400
Cantilever thickness	Mask M-2	200-250
Pyramid size top	Mask M-1	1072
Pyramid size base	Mask M-1	1450
CCCS outer rectangle	Mask M-1	2000
V-groove width	Mask F-1	1142
V-groove length	Mask F-1	1900



**Figure 4.14** Detailed view of Mask M-1 with overlapped Masks M-2 and F-1



**Figure 4.15** Detailed view of Mask M-2 with overlapped Masks M-1 and F-1



**Figure 4.16** Detail of Mask F-1 with overlapped Masks M-1 and M-2

# Chapter 5

## MICROFABRICATION

### 5.1 Fabrication processes

The fabrication and testing of the wafer passive alignment features was done at the Microelectronics Technology Lab (MTL) at MIT.

Common microelectronics processes, such as photolithography, thin film deposition, plasma etching and wet anisotropic etching were used to create the passive alignment features. The shallow plasma etches were masked with thin ( $1\mu\text{m}$ ) photoresist. The deep wet anisotropic etches were masked with a patterned  $2000\text{\AA}$  thin silicon nitride film. Deep Reactive Ion Etch (DRIE), a variant of the reactive ion etch process, capable of achieving very high aspect ratio and directional etches, was used to release the cantilever flexures. Thick ( $10\mu\text{m}$ ) photoresist was used to mask the DRIE step. Four inch, double sided polished, (100) wafers were used for both convex and concave features.

A detailed process flow for both convex and concave features, is given in Appendix A. The masks are shown in Appendix B. Sections 5.1.1 and 5.1.2 discuss the micro-fabrication process of the convex and concave coupling features respectively.

### 5.1.1 Concave coupling features

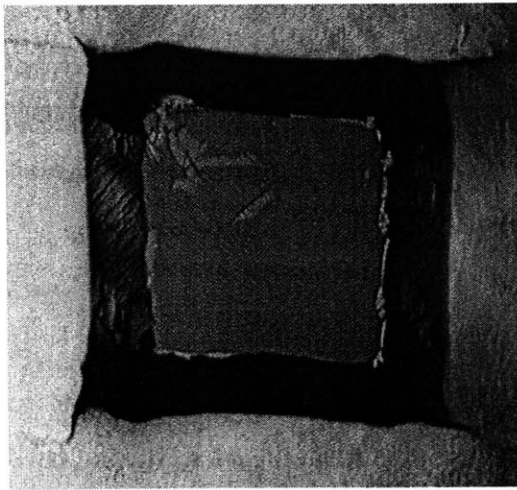
Alignment marks (Mask A) were plasma etched (HCl & HBr recipe) on the front side of 4 inch, double side polished, (100) silicon wafers. These alignment marks were later used to quantify the repeatability and accuracy of the passive wafer alignment.

After stripping the photoresist and preparing the wafers for deposition with an RCA clean, 2000Å of silicon nitride were deposited through low pressure chemical vapor deposition (LPCVD). The nitride was patterned on the wafer back side (Mask M-1) with a CF<sub>4</sub> plasma etch. After stripping the photoresist mask, the wafers were etched in a 20% weight KOH solution in de-ionized (DI) water at 85°C. This created the pits defining the cantilever height and the pyramids. A post KOH clean and nitride strip followed. Thick (10 μm) photoresist was spun and patterned (Mask M-2) on the wafer front side. For the front-side spin casting, a piece of punctured die saw tape was placed between the vacuum chuck and the wafer. The tape directed the vacuum to the center of the wafer, away from the KOH etched pits. The device wafer was then mounted on a 4-inch handle wafer using thick photoresist. The wafer stack was etched in DRIE until the device cantilevers had been released. The wafers were demounted using acetone and put in the asher to burn off any photoresist traces and the teflon deposited by the DRIE process during the passivation cycles.

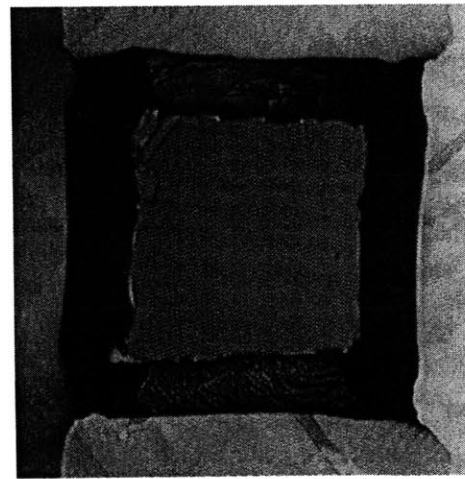
It was critical for the fabrication of the convex alignment features, to maintain the DRIE etch-rate constant over the whole wafer, so all cantilevers would be released simultaneously. The back side of the wafers are not protected with photoresist. Any etch after puncture of the wafer, would expose the unprotected wafer back side, causing damage to the pyramids. The etch rate of silicon in DRIE is strongly dependant on the aspect ratio of the etch; thus, a wider trench will etch faster then a narrow one. A halo mask was used in Mask M-2 to maintain the etch line-width constant throughout the wafer. The halo mask was snapped off before testing.

A slight over-etch, (approximately 30  $\mu\text{m}$  deep) was needed to fully release all cantilevers, due to plasma non-uniformity and slightly faster etch rate on the wafer outside diameter than in the center of the wafer.

Initially, stoichiometric silicon nitride was deposited on the wafers to mask the KOH etch. It was assumed, the higher density silicon nitride would provide a better mask for the KOH etch. The high residual stress of the stoichiometric silicon-nitride, however, caused the nitride mask to break off as the convex compensating structures were being under-etched. It is assumed, that the constant mask change caused the pyramid edges to become jagged and the pyramid faces to become rough. Figures 5.1 and 5.2 show optical microscope pictures of the pyramids masked with stoichiometric nitride. Note that the  $\{100\}$ - $\{111\}$  interface is very jagged, and that the surface finish of the pyramid faces is very rough. Plasma enhanced chemical vapor deposition (PCVD) silicon nitride is deposited at a lower temperature, and thus has significantly lower residual stress than stoichiometric silicon nitride. PCVD silicon nitride was used to mask the KOH etch, eliminating the rough



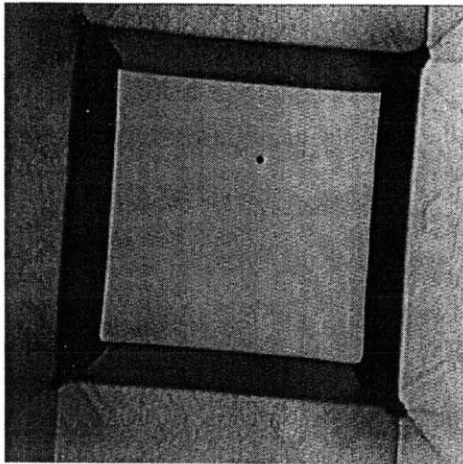
**Figure 5.1** Pyramid masked with stoichiometric silicon-nitride, the thin film residual stress caused jagged edges and rough surface finish



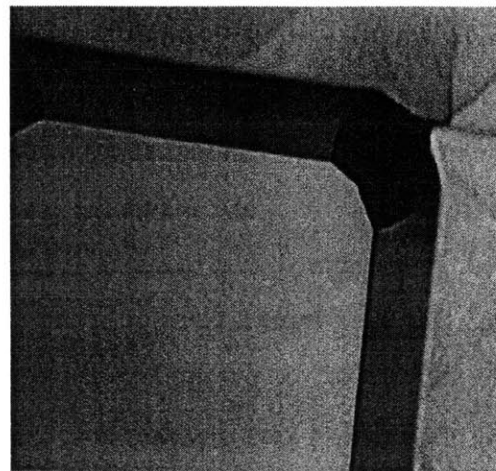
**Figure 5.2** Detail of stoichiometric silicon-nitride masked pyramid, showing jagged edges and rough surface finish

surface-finish of the pyramid walls. Figures 5.3 and 5.4 show optical microscope images

of the pyramids masked with PCVD silicon nitride. Notice the pyramid definition and significantly better surface finish.



**Figure 5.3** Pyramid masked with CVD silicon-nitride, shown after nitride strip. The low residual stress film yields sharp edges and smooth sidewalls after the KOH etch



**Figure 5.4** Detail of CVD silicon-nitride masked pyramid after KOH etch. Picture taken after nitride strip.

Figures 5.5 and 5.6 show SEM pictures of the convex alignment features after release and removal of the halo-mask. Notice the presence of small corner structures. These are traces of the corner compensating structures, which were under-etched. In a second run, the wafers were over-etched to eliminate these corner structures. Figures 5.7 and 5.8 show SEM pictures of the second run structures after removal of the halo mask. .

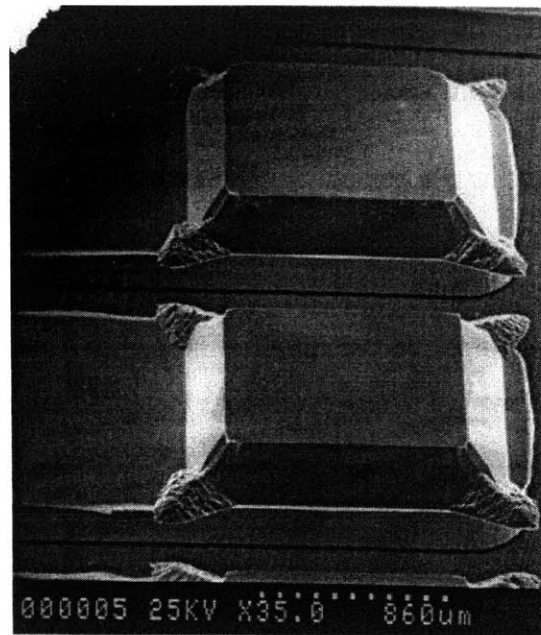
### 5.1.2 Concave coupling features

Alignment marks (Mask A) were plasma etched (HCl & HBr recipe) on the back side of 4 inch, double side polished, (100) silicon wafers. These alignment marks were later used to quantify the repeatability and accuracy of the passive wafer alignment.

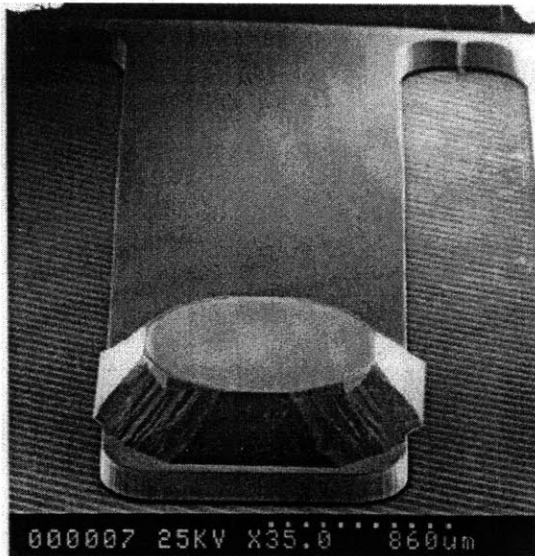
After stripping the photoresist and preparing the wafers for deposition with an RCA clean, 2000Å of silicon nitride were deposited through LPCVD. The silicon nitride was patterned on the wafer front side (Mask F-1) with a CF<sub>4</sub> plasma etch. After stripping the pho-



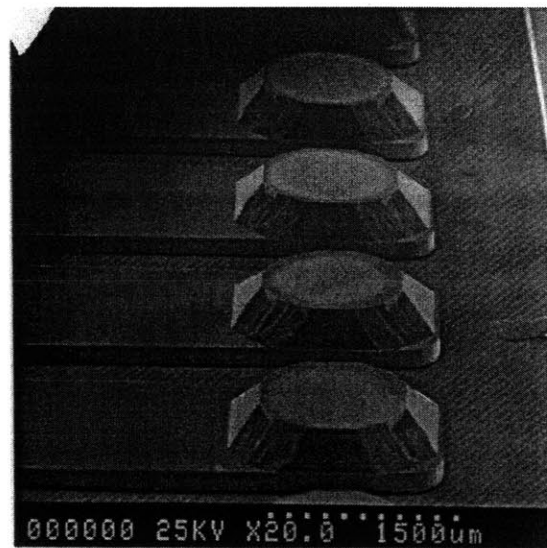
**Figure 5.5** Front view SEM image of the convex coupling feature, (wafer 1). Traces of the convex corner compensating structures can be seen on the lower corners of the pyramid



**Figure 5.6** SEM side view image of the convex coupling feature array, (wafer 1)



**Figure 5.7** Front view SEM image of the convex coupling feature after release (wafer 2)

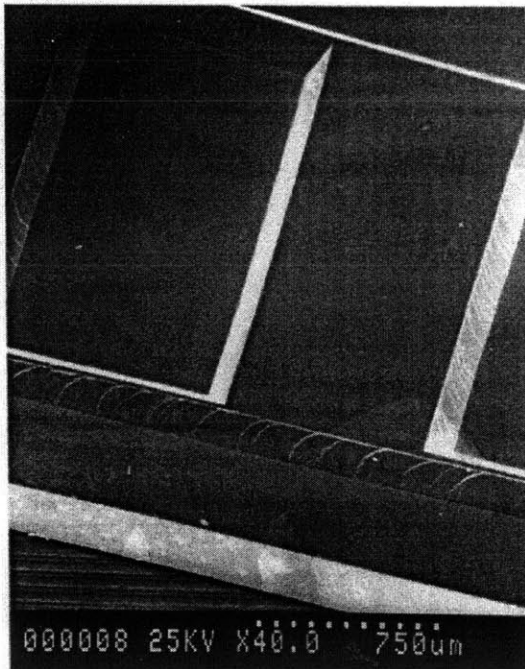


**Figure 5.8** SEM side view image of the convex coupling feature array (wafer 2)

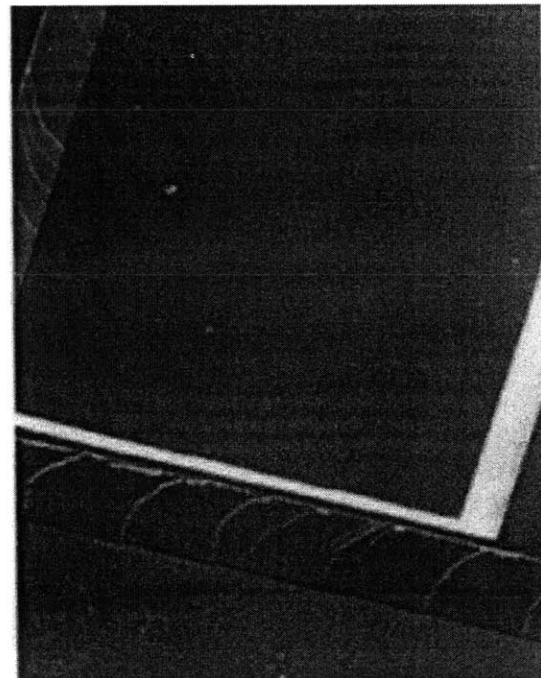
toresist mask, the wafers were etched 150  $\mu\text{m}$  deep in a 20% weight KOH solution at 85°C. The etch exposed the concave feature boss and V-grooves. A post KOH clean and silicon nitride strip followed.

The plasma etcher uses brackets that hold the wafer in place. These brackets cause a shadow effect keeping the silicon-nitride underneath the bracket from being etched. The under-etched spots leave unwanted “island” structures after the KOH etch. These structures keep the convex and the concave coupling features from fully engaging when the wafers are stacked, and were therefore removed with the diesaw, by cutting off the wafer edges.

Figures 5.9 and 5.10 show SEM pictures of the convex wafer alignment features. Note that since stoichiometric nitride was used to mask the KOH etch, the pyramid walls are rough and the edges jagged.



**Figure 5.9** SEM picture of concave feature boss and V-groove



**Figure 5.10** Detail of boss and V-groove, showing rough surface finish on the boss and V-groove side-walls



## 5.2 Process optimization: Convex corner compensating structures

Many techniques have been proposed to add material to the masks of wet anisotropic etches, in order to compensate for bevelling at convex corners, i.e. [23]-[25]. Zhang [25] proposes a particularly small convex corner compensating structure (CCCS) and gives equations to size these structures according to the depth of the etch, etch rates and anisotropy ratio. There are however no equations that predict the exact etch rates and anisotropy of a wet anisotropic etches as a function of temperature and solution concentration [26]. An experiment was run to optimize the size of the CCCS for the KOH solution (concentration and temperature) used at MTL.

Zhang [25] proposes the following relationships to mask the convex corners:

$$\frac{V_{\langle 411 \rangle}}{V_{\langle 100 \rangle}} D_e = 0.857(0.424B - 0.4g + 0.4(M + g)) \quad 5.1$$

where  $V_{\langle 411 \rangle}$  is the etch rate in  $\langle 410 \rangle$ ,  $V_{\langle 100 \rangle}$  is the etch rate in  $\langle 100 \rangle$ ,  $D_e$  is the etch depth, and  $B$ ,  $M$ , and  $g$  are the dimensions which define the geometry of the CCCS, as shown in Figure 5.11.

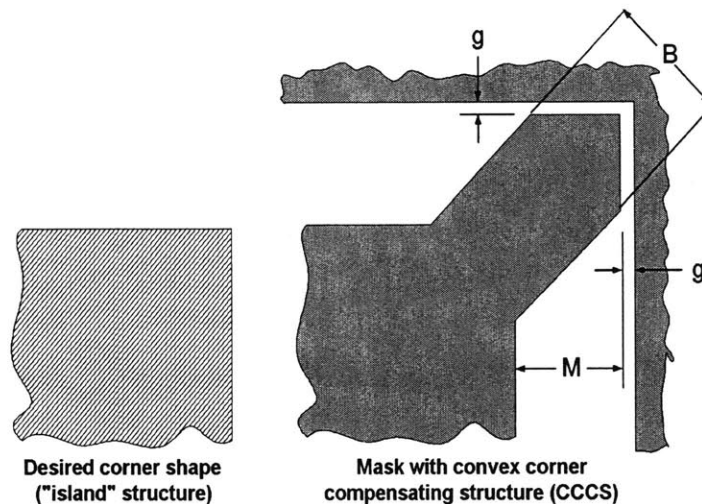


Figure 5.11 Dimensions of the CCCS, after Zhang [25]

$V_{\langle 410 \rangle} / V_{\langle 100 \rangle}$ , the anisotropy ratio, is KOH concentration dependent, and ranges from 1.3 to 1.6 for 15 - 50% weight concentration. An anisotropy ratio of 1.4 is assumed for the 20% weight KOH solution used. The gap between masks  $g$  is constrained by the minimum feature size the mask is capable of reproducing. In the case of Masks M-1, M-2 and F the minimum feature size is 20  $\mu\text{m}$ . These masks are made by a photolithography step using a high quality transparency print.

Table 5.1 presents the CCCS dimensions determined from equation 5.1 for different etch depths. The dimensions labeled as “nominal” were calculated using equation 5.1. The dimensions labeled as “110% size” and “90% size” were scaled 10% larger, and 10% smaller in size respectively. The dimensions are defined in Figure 5.12.

**TABLE 5.1** CCCS dimensions for various etch depths, applying equation 5.1

Group	Dimension	300 $\mu\text{m}$	350 $\mu\text{m}$	400 $\mu\text{m}$
Nominal dimensions	M [ $\mu\text{m}$ ]	442	512	582
	B [ $\mu\text{m}$ ]	758	885	1011
	a [ $\mu\text{m}$ ]	536	625	715
	b [ $\mu\text{m}$ ]	978	1137	1297
	CL width [ $\mu\text{m}$ ]	1975	2294	2614
110% size	M [ $\mu\text{m}$ ]	486	563	640
	B [ $\mu\text{m}$ ]	834	973	1112
	a [ $\mu\text{m}$ ]	590	688	786
	b [ $\mu\text{m}$ ]	1075	1251	1427
	CL width [ $\mu\text{m}$ ]	2127	2522	2873
90% size	M [ $\mu\text{m}$ ]	397	461	524
	B [ $\mu\text{m}$ ]	682	796	910
	a [ $\mu\text{m}$ ]	483	563	643
	b [ $\mu\text{m}$ ]	880	1024	1167
	CL width [ $\mu\text{m}$ ]	1780	2067	2354

Three die of each group and etch depth combination were patterned on (100) silicon wafers as shown in figure 5.13. One of the three dies was etched to the target depth shown in table 5.1. The two others were over and under etched 10% of the calculated target time respectively. The combinations run in the experiment are shown in Table 5.2. The width of the pyramid corner bevelling for each combination was measured with a microscope. Table 5.3 presents the results. Figures C1 to C10 in Appendix C show SEM pictures of a few sample dies.

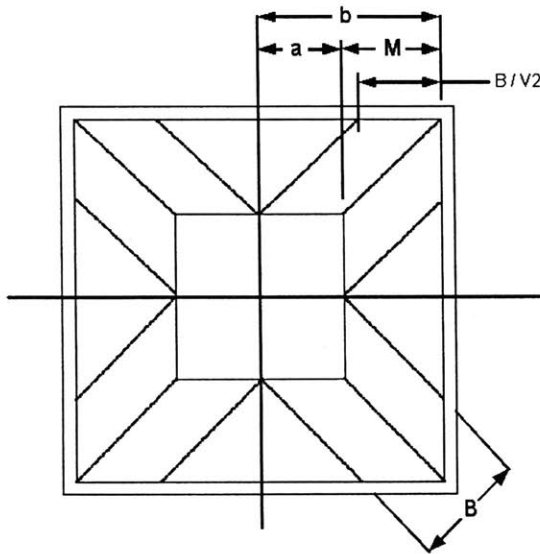


Figure 5.12 CCCS dimensions for pyramid masking

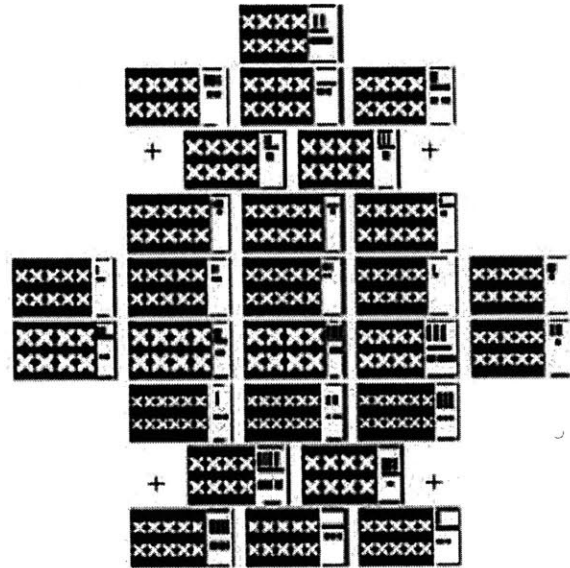


Figure 5.13 CCCS experiment mask

TABLE 5.2 CCCS sizing experiment combinations

Feature sizes	300 $\mu\text{m}$	300 $\mu\text{m}$ + $\Delta T$	300 $\mu\text{m}$ - $\Delta T$	350 $\mu\text{m}$	350 $\mu\text{m}$ + $\Delta T$	350 $\mu\text{m}$ - $\Delta T$	400 $\mu\text{m}$	400 $\mu\text{m}$ + $\Delta T$	350 $\mu\text{m}$ - $\Delta T$
Nominal	A1	B1	C1	D1	E1	F1	G1	H1	I1
110% size	A2	B2	C2	D2	E2	F2	G2	H1	I2
90% size	A3	B3	C3	D3	E3	F3	G3	H1	I3

TABLE 5.3 CCCS sizing experiment results

Under-etched	Die	Etch depth [μm]	Undercut at pyramid base [μm]	Undercut at pyramid top [μm]
	A1	300	15	10
	A2	300	5	0
	A3	315	25	10
	B1	328	30	15
	B2	408	25	12.5
	B3	384	35	20
*	C1	243	-5	-2.5
*	C2	290	-10	-7.5
	C3	247	10	7.5
	D1	400	20	15
*	D2	327	-5	-25
	D3	385	25	10
	E1	432	25	12
	E2	402	2.5	0
	E3	407	35	20
*	F1	266	-5	0.25
*	F2	250	-10	5
	F3	285	0	0
	G1	400	5	10
*	G2	384	-5	-2.5
	G3	410	30	15
	H1	423	40	22
	H2	392	0	0
	H3	412	45	20
*	I1	376	-7.5	-5
*	I2	393	-15	-7.5
	I3	300	5	10

The goal is to find the CCCS size of a fully etched or over etched die, that has the least corner bevelling and variation in case of an over/under etch. All under etched die are not

considered since the remaining corner structures would affect the engagement of concave and convex alignment structures. Die A is selected as the optimum geometry for the KOH etch to be used.



# Chapter 6

## TESTING AND RESULTS

Testing of the passive wafer alignment structures was performed at the MTL on an Electronics Vision Group™ TBM8 measurement system.

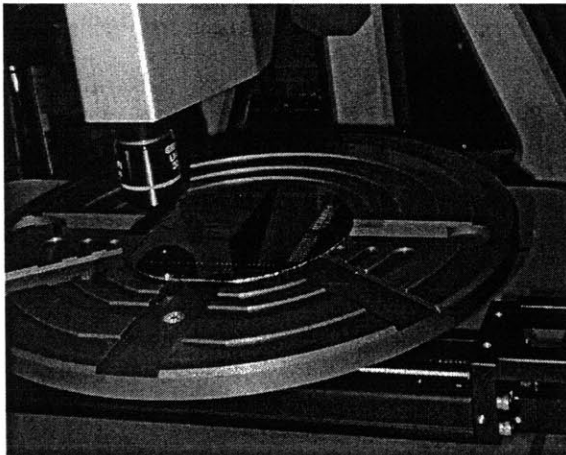
The TBM8 consists of a rotating wafer chuck base and an optical system that displays a magnified picture of the wafer front and back side simultaneously on a monitor. The TBM8 takes advantage of an error doubling effect when the front to back side measurements are taken 180 degrees from each other. After placing a wafer with both sides patterned, or in our case the two mating wafers, a hair-line pointer is placed over the alignment marks of the wafer front and back side. The base is rotated 180 degrees, and the process of placing the hair-line pointer over the alignment marks is repeated. The front-to-back side misalignment is calculated based on the relative position at which the hairline markers were placed. Figure 6.1 shows the test set-up used. Notice the mating wafers are mounted on the TBM8 wafer chuck. Displayed on the screen, are the top and bottom wafer alignment marks. Figures 6.2 and 6.3 show close-up views of the self-aligned wafers on the vacuum chuck.

### 6.1 Testing sequence

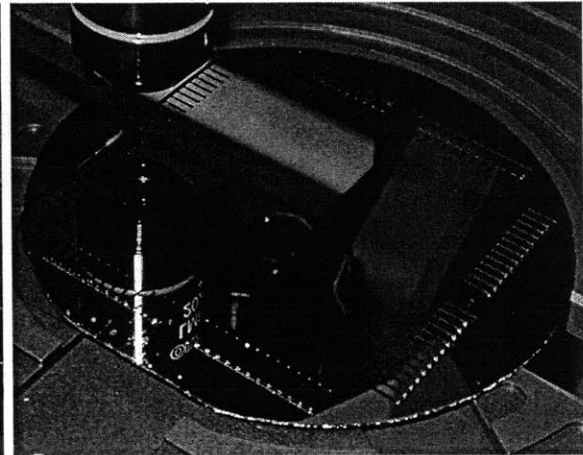
The wafer with concave features was put on the TBM8 with the features facing up. The wafer with convex features was placed on top of the wafer with concave features, facing down, with the major flat pointing in the machine's negative "y" direction, as shown in



**Figure 6.1** Measurement set-up used to test the passive wafer alignment features. Electronics Vision TBM8



**Figure 6.2** Wafer chuck and top CCD objective. The measurement coordinate system is indicated



**Figure 6.3** Detailed view of passive wafer aligned stack. Note the cantilevers and bottom wafer showing on the left side of the stack

Figure 6.3. The two wafers were aligned roughly and tapped lightly to enable the wafer alignment features to engage and self-align the wafers. After the top wafer had reached a stable position (i.e. would not move when tapped lightly), the front-to-back side alignment accuracy was measured following the sequence described previously.



## 6.2 Determination of the measurement system noise

A “cap” test was performed to estimate the noise of the measurement system. Two wafers with mating passive alignment features were placed on the TBM8, as described previously. The base was tapped lightly, and after the top wafer had reached a stable position, a mass was placed on the wafer stack to preload the wafer coupling and keep the top wafer from moving relative to the bottom one between measurement cycles, when the vacuum was lost. The alignment accuracy was repeatedly measured without taking the wafers off the fixture. Table 6.1 presents the results for a 20 cycle run. The average accuracy value for X and Y is given, as well as the length of the error vector, and its angle. The error vector is the linear distance between the top and bottom alignment marks. The repeatability is calculated as the range of the data, after removing the outlier values<sup>1</sup>. The complete experimental data for the cap test is shown in Table D1 of Appendix D.

**TABLE 6.1** Cap test results, wafers M-1 & F-1, preloaded

	X [ $\mu\text{m}$ ]	Y [ $\mu\text{m}$ ]	Error [ $\mu\text{m}$ ]	Error Angle [deg]
Average accuracy	0.36	-5.31	5.33	-86.28
Repeatability	0.42	0.42	0.42	2.55

The cap test shows sub-micrometer repeatability of the measurement system.

## 6.3 Repeatability and accuracy results of passive wafer alignment

Two wafers with patterned convex features, M1 and M2, and two wafers with patterned concave features F1, F2 were tested. Wafer M1 was slightly under etched, so traces of the CCCS were still present on the corners of the pyramid at the base, as shown in Figures 5.5 and 5.6. Wafer M2 was over etched to eliminate the CCCS traces on the corner of the pyr-

1. Outlier are extreme values, i.e highest and lowest readings

amids. Figures 5.7 and 5.8 show detailed views of the pyramids. Both concave wafers F1 and F2 were etched to the same depth.

The repeatability and accuracy of the wafer passive alignment was measured for a 20 cycle sequence, using wafers M2 and F1 with the only preload being the top wafers mass. The results are presented in table 6.2. The complete data for this experiment is shown in Table D2 of Appendix D. The overall repeatability value is around  $1\mu\text{m}$ . The accuracy is  $1.4\mu\text{m}$ . Compared to the cap test, the alignment accuracy is significantly better. The offset

**TABLE 6.2** Test results Wafers M-2 & F-1, all cantilevers

	X [ $\mu\text{m}$ ]	Y [ $\mu\text{m}$ ]	Error [ $\mu\text{m}$ ]	Error Angle [deg]
Average accuracy	0.88	-1.08	1.41	-50.2
Repeatability	0.63	1.06	1.06	32.47

seen is assumed to be caused mainly by the alignment of masks M-1, M-2 and F during the photolithography steps. Since these masks were made from emulsion transparencies, with a minimum feature size of  $20\mu\text{m}$ , such an offset seems reasonable.

#### **6.4 Repeatability and accuracy as a function of number of contact points: the elastic averaging effect**

The same test sequence was repeated with wafers M-1 and F-1. To verify a relationship between the alignment repeatability and the number of contact points, a cantilever from each array, starting at the wafer OD and working towards the center, was snapped off after each 20 cycle run. The measurements are presented in Table 6.3. The complete experimental data for this experiment is shown in Tables D3 through D9, of the Appendix D.

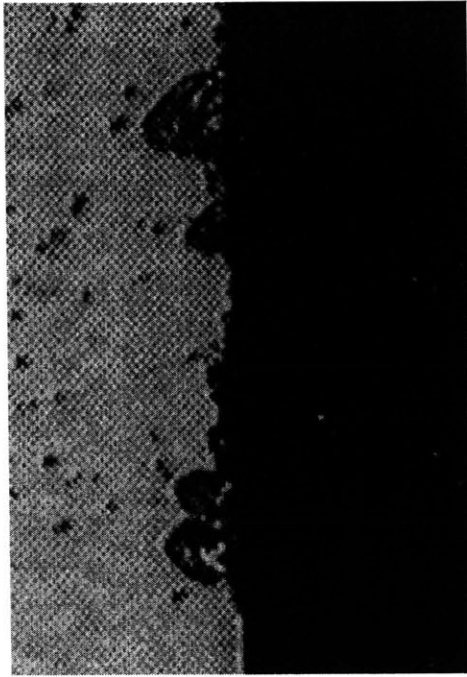
Repeatability of less than  $1\mu\text{m}$  was measured in several cases. There was however no trend to be seen, neither in the repeatability, nor on the accuracy of the alignment. Figures 6.4 and 6.5 show pictures taken from the convex structures after performing the test. Wit-

**TABLE 6.3** Test results wafers M-1 & F1, no preload besides top wafer mass

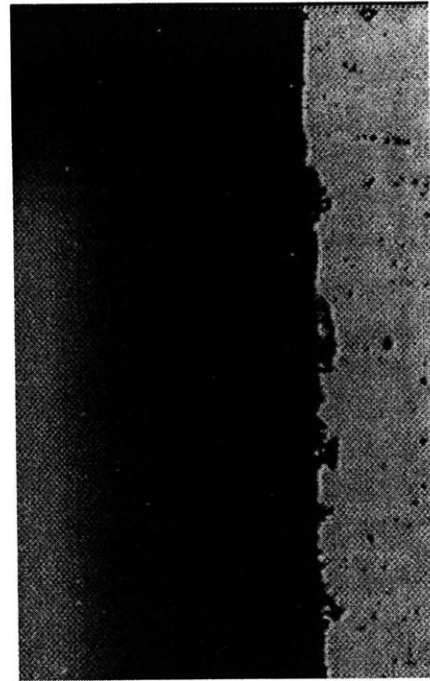
	<b>Total number of cantilevers</b>	<b>X [<math>\mu\text{m}</math>]</b>	<b>Y [<math>\mu\text{m}</math>]</b>	<b>Error  [<math>\mu\text{m}</math>]</b>	<b>Error Angle  [deg]</b>
Average accuracy	96	-0.11	-5.56	5.63	-0.01
Repeatability	96	2.31	0.21	0.34	175
Average accuracy	88	-0.16	-5.81	5.88	26.46
Repeatability	88	2.94	0.27	0.39	173
Average accuracy	80	1.24	-6.51	6.81	-11.49
Repeatability	80	3.35	0.68	1.19	157.59
Average accuracy	72	2.46	-6.90	7.34	-70.45
Repeatability	72	0.42	0.63	0.59	4.81
Average accuracy	64	-4.25	-9.76	10.68	66.56
Repeatability	64	1.67	0.63	0.93	7.53
Average accuracy	56	-4.32	-9.02	10.04	64.4
Repeatability	56	0.42	0.84	0.57	3.28
Average accuracy	48	-5.19	-7.54	9.16	55.77
Repeatability	48	2.85	2.11	3.08	11.08

ness marks could be seen on the edges of the v-grooves left by the corner structures on the pyramids. Figures 6.4 and 6.5 show detailed views of some of the v-grooves. Based on the witness marks left, the pyramid was probably not properly seated in the V-groove.

The same experiment was repeated with wafers M-2 and F-2. The results are presented in Table 6.4. The complete test data for this experiment is presented in Tables D10 through D21 of Appendix D. The overall repeatability is mostly less than  $1\mu\text{m}$ . The accuracy



**Figure 6.4** Detail of V-groove damage after M-1 & F1 wafer testing



**Figure 6.5** Detailed of V-groove damage after M-1 F-1 wafer testing. The shadowed area is the tapered sidewall of the V-groove

remains almost constant, with an error vector of  $7\ \mu\text{m}$ . It was expected, that the accuracy and repeatability be best in the beginning of the test, and drop as cantilevers were being snapped off. This however, was not the case. It is assumed that the preload is too small so not all coupling features are engaged, and thus the averaging effect is not noticeable. On the other hand, the accuracy of the measurement system is not significantly larger than the value measured, so it is possible that the system noise make the trend unnoticeable.

The large discrepancy between the repeatability values and the accuracy, is due to an offset caused by the tolerance stack up of the individual wafers and the photolithographic steps used to pattern the features on the wafers. Although the alignment marks themselves are  $3\ \mu\text{m}$  wide, Masks M-1, M-2, and F were made from emulsion transparencies, which have a minimum feature size of  $20\ \mu\text{m}$ . Alignment to these masks caused an offset which was later observed when testing the wafer passive alignment features.

**TABLE 6.4** Test results wafers M-2 & F-2, no preload besides top wafer mass

	<b>Total number of cantilevers</b>	<b>X [<math>\mu\text{m}</math>]</b>	<b>Y [<math>\mu\text{m}</math>]</b>	<b>Error [<math>\mu\text{m}</math>]</b>	<b>Error Angle [deg]</b>
Average accuracy	96	-6.93	1.35	7.07	-11.15
Repeatability	96	1.09	0.43	1.12	3.16
Average accuracy	88	-6.26	0.75	6.3	-6.52
Repeatability	88	0.84	0.78	0.87	6.86
Average accuracy	80	-7.29	0.44	7.29	-3.63
Repeatability	80	0.84	0.84	0.84	6.60
Average accuracy	72	-1.68	4.52	4.83	-69.67
Repeatability	72	-1.04	0.85	1.01	12.40
Average accuracy	64	-4.3	-5.86	7.22	53.86
Repeatability	64	.43	0.42	0.43	3.56
Average accuracy	56	-5.99	-4.26	7.37	35.51
Repeatability	56	0.63	0.21	0.46	3.19
Average accuracy	48	-6.55	-4.21	7.82	32.91
Repeatability	48	0.63	0.42	0.52	5.22
Average accuracy	40	-6.46	-3.69	7.42	30.06
Repeatability	40	0.42	0.63	0.68	5.79
Average accuracy	32	-4.61	-5.43	7.32	49.87
Repeatability	32	0.63	1.05	0.89	8.12

**TABLE 6.4** Test results wafers M-2 & F-2, no preload besides top wafer mass

	<b>Total number of cantilevers</b>	<b>X [<math>\mu\text{m}</math>]</b>	<b>Y [<math>\mu\text{m}</math>]</b>	<b>Error [<math>\mu\text{m}</math>]</b>	<b>Error Angle [deg]</b>
Average accuracy	24	-7.56	-3.87	8.53	27.16
Repeatability	24	0.84	1.05	0.67	7.59
Average accuracy	16	-7.51	-4.77	8.89	32.45
Repeatability	16	0.42	0.64	0.58	3.53
Average accuracy	8	-7.14	-4.77	8.89	32.45
Repeatability	8	0.42	0.89	0.47	6.20

# Chapter 7

## CONCLUSIONS AND FUTURE WORK

Various macro-scale precision alignment techniques were presented and evaluated for their application feasibility in aligning wafers. A passive wafer alignment technique, as well as the process to bulk micro machine the features on silicon, that enable the passive alignment were developed. The coupling features were fabricated and tested.

Testing shows that sub micrometer repeatability and one micrometer accuracy is indeed feasible with the proposed technique. The elastic averaging effect, as a function of number of contact points was evaluated, but the results are inconclusive, most likely due to the level of noise in the measurement system and the lack of preload needed to force all passive alignment features to engage. Nevertheless the results are impressive, specially considering that 20  $\mu\text{m}$  feature size masks were used to pattern the features.

The tests show that using as little as two alignment features per wafer edge yields sub-micrometer repeatability. The size of the alignment features can be optimized to reduce the lost wafer area.

It is important to mention that the processes used to create the wafer alignment features restrict further processing. The wet anisotropic etch leaves the etched (100) too rough for anodic bonding. Other bonding processes however, such as eutectic bonding could be used. Hence, now that the basic strategy has been developed, better manufacturing methods need to be developed and tested.

The results of this research are a proof of concept that macro-scale precision alignment techniques can indeed be applied to align wafers to each other with high precision.

Further testing using traditional, e-beam written masks, should be performed to make a better evaluation of the accuracy limitations of this passive wafer alignment technique.



# REFERENCES

- [1] Stephen D. Senturia, *Microsystem Design*, Kluwer Academic Publishers, Boston, MA 2000. page 161
- [2] Douglas R. Sparks, *Packaging for Harsh Environments*, IEEE Instrumentation & Measurement Magazine, September 2001, pages 30-33
- [3] J. -Q. Lü, et al, *Stacked Chip-to-Chip Interconnections Using Wafer Bonding Technology with Dielectric Bonding Glues*, Interconnect Technology Conference, 2001. Proceedings of the IEEE 2001 International, pages 219-221
- [4] A. R. Mirza, *One micron precision, wafer-level aligned bonding for interconnect, MEMS and packaging applications*, Electronic Components & Technology Conference, 2000. IEEE. , pages 676-680
- [5] Y. Bäccklund, *Micromechanics in optical microsystems-with focus on telecom systems*, J. Micromech. Microeng. 7 , 1997, Pages 93-98
- [6] C. Strandman, et al, *Passive and fixed alignment of devices using flexible silicon elements formed by selective etching*, J. Micromech. Microeng. 8 , 1998, Pages 39-44
- [7] R. M. Bostock, et al, *Silicon nitride microclips for the kinematic location of optic fibres in silicon V-shaped grooves*, J. Micromech. Microeng. 8 , 1998, Pages 343-360
- [8] A. H. Slocum, *Kinematic couplings for precision fixturing-Part 1: Formulation of design parameters*, Precision Engineering ,1998, VOL. 10, No. 2, pages 85-91
- [9] A. H. Slocum, *Design of three-groove kinematic couplings*, Precision Engineering, April 1992, Vol 14, No. 2, pages 67-76
- [10] A. H. Slocum, et al, *Flexural mount kinematic couplings and method*, US patent 5,678,944, October 1997
- [11] A. H. Slocum, Engineering Design, in chapter 11 Handbook of Mechanical Engineering, 1999, CRC Press LLC, page 76
- [12] W. R. Moore, *Foundations of mechanical accuracy*, Moore Special Tool Company, Bridgeport Connecticut,1970, pages 233-235
- [13] G. K. Christiansen, *Toy building brik*, US patent 3,005,282, October 1961

- [14] G. K. Christiansen, *Toy building sets and building blocks*, US patent 3,034,254, May 1962
- [15] A. H. Slocum, *Precision Machine Design*, Society of Manufacturing Engineers, Dearborn Michigan, 1992, pages 120-123
- [16] Kos Ishii, *Introduction to Design of Manufacturability*, Design for Manufacturability: Product Definition, Notes for ME-217A in Department of Mechanical Engineering at Stanford University, January 2002, Section 2.1, page 3
- [17] Eun-Hyun Park, et al, *Microlens for efficient coupling between LED and optical fiber*, IEEE Photonics Technology Letters, April 1999, Vol 11, No. 4, page 439-441.
- [18] N. Kaou, et al, *Microconnectors for the passive alignment of optical waveguides and ribbon optical fibers*, MEMS 2000, IEEE Thirteenth Annual International Conference on Micro Electro Mechanical Systems, pages 692 -697
- [19] Yvla Bäcklund, *Micromechanics in optical microsystems-with focus on telecom systems*, J. Micromech. Microeng., 7, 1997, pages 93-98
- [20] Carola Strandman, et al, *Passive and fixed alignment of devices using flexible silicon elements formed by selective etching*, J. Micromech. Microeng., 8, 1998, pages 39-44
- [21] R. M. Bostock, *Silicon nitride microclips for the kinematic location of optic fibres in silicon V-shaped grooves*, J. Micromech. Microeng. , 8, 1998, pages 346-360
- [22] Nam Suh, *Axiomatic Design: Advances and Applications*, Oxford university Press, New York, 2000, pages 5
- [23] Henning Schroeder, et al, *Convex corner undercutting of {100} silicon in anisotropic KOH etching: The new step-flow model of 3-D structuring and first simulation results*, Journal of Microelectromechanical Systems, Vol 10, No. 1, 2001, pages 88-97
- [24] H. Sandmaier, et al, *Corner compensation techniques in anisotropic etching of (100)-Silicon using aqueous KOH*, Tech. Digest, 7th International Conference Solid-State Sensors and Actuators (Transducers 1991), San Francisco, CA, 1991, pages 456-459
- [25] Qingxin Zhang, et al, *A new approach to convex corner compensation for anisotropic etching of (100) Si in KOH*, Sensors and Actuators, A, 56, 1996, pages 251-254
- [26] Gregory Kovacs, et al, *Bulk micromachining of silicon*, Proceedings of the IEEE,

Vol. 86, No. 8, August 1998, pages 1536-1551

||

# **Appendix A**

## **PROCESS SEQUENCE**

TABLE A.1 Concave coupling process

Step	Lab	Machine	Recipe	Description
0	TRL	Acidhood	Piranha, HF dip	Pre-metal clean
1.1	TRL	HMDS	-	P.R. adhesion promoter
1.2	TRL	Coater	1 $\mu$ m	Coat with 1 $\mu$ m positive P.R. (wafer back side)
1.3	TRL	Pre-bake oven	90 deg C, 30 min	Pre-bake P.R.
2	TRL	EV1	-	Expose alignment marks (Mask-A)
3	TRL	Photo wet-1 (non-Au)	1-2 min	Develop P.R.
4	TRL	Post-bake oven	30 min	Post-bake P.R.
5	ICL	AME5000	SF6, 85s	Etch Si, (wafer back side)
6	ICL	Asher	-	Strip P.R.
7	ICL	RCA-hood	Std.	RCA clean
8	ICL	Tube A-5	-	Deposit Nitride (2000A)
9.1	TRL	HMDS	-	P.R. adhesion promoter
9.2	TRL	Coater	1 $\mu$ m	Coat with 1 $\mu$ m positive P.R. (wafer front side)
9.3	TRL	Pre-bake oven	90 deg C, 30 min	Pre-bake P.R.
10	TRL	EV1	-	Expose Mask-F (front side, aligning to back side)
11	TRL	Photo wet-1 (non Au)	1-2 min	Develop P.R.
12	TRL	Post-bake oven	30 min	Post bake P.R.
13	ICL	AME5000	CF4-16s, SF6-85 s	Pattern nitride
14	ICL	Asher	2 min	Strip P.R.
15	EML	KOH hood (non Au)	KOH, 7.8 h	Anisotropic etch (timed)
16	TRL	Acidhood	2XPiranha, Hf dip	Post KOH etch clean
17	TRL	Acidhood	Transetch-N	Strip nitride

TABLE A.2 Convex coupling process

Step	Lab	Machine	Recipe	Description
0	TRL	Acidhood	Piranha, HF dip	Pre-metal clean
1.1	TRL	HMDS	-	P.R. adhesion promoter
1.2	TRL	Coater	1 $\mu$ m	Coat with 1 $\mu$ m positive P.R. (wafer front side)
1.3	TRL	Pre-bake oven	90 deg C, 30 min	Pre-bake P.R.
2	TRL	EV1	1.5s	Expose alignment marks (Mask-A)
3	TRL	Photo wet-1 (non-Au)	1.5 min	Develop P.R.
4	TRL	Post-bake oven	120 deg C, 30 min	Post-bake P.R.
5	ICL	AME5000	Chamber B, HCl+HBr	Etch Si, (alignment marks, wafer front side)
6	ICL	Acidhood	Piranha	Strip P.R.
7	ICL	RCA-hood	Std.	clean for Diffusion Tube / Concept-1
8	ICL	Tube A-5 / Concept-1	2000A Si <sub>3</sub> N <sub>4</sub>	Deposit Silicon Nitride
9.1	TRL	HMDS	-	P.R. adhesion promoter
9.2	TRL	Coater	1 $\mu$ m	Coat with 1 $\mu$ m positive P.R. (wafer back side)
9.3	TRL	Pre-bake oven	90 deg C, 30 min	Pre-bake P.R.
10	TRL	EV1	1.5s	Expose Mask-M-1 (wafer back side)
11	TRL	Photo wet-1 (non Au)	1.5 min	Develop P.R.
12	TRL	Post-bake oven	30 min	Post bake P.R.
13	ICL	AME5000	CF <sub>4</sub> 55s	Pattern nitride
14	TRL	Acidhood	Piranha Clean	Strip P.R.
15	ICL*	KOH hood (non Au)	KOH, 3h 45 min (300 $\mu$ m deep), 25% weight, 85C	Anisotropic etch (timed)
16.1	TRL	Acidhood	Piranha clean (yellow tank)	Post KOH clean

TABLE A.2 Convex coupling process

Step	Lab	Machine	Recipe	Description
16.2	TRL	Acidhood	Piranha clean (green tank)	Post KOH clean
16.3	TRL	Acidhood	HF dip	Post KOH clean
17	TRL	Acidhood	Trans etch-N	Strip nitride
18.1	TRL	HMDS	-	P.R. adhesion promoter
18.2	TRL	Coater	10 $\mu\text{m}$ (thick P.R.)	Coat with 10 $\mu\text{m}$ (thick P.R., wafer front side)
19	TRL	Pre-bake oven	90C, 60 min	Pre-bake
20	TRL	EV1	22s	Expose Mask M-2
21	TRL	Photo wet-1 (non-Au)	3-4 min	Develop P.R.
22	TRL	Pre-bake oven	90C, 30 min	Post-bake after develop
23	TRL	-	-	Mount on 4'' handle wafer (front side up)
24	TRL	STS-1	100 $\mu\text{m}$ deep etch	DRIE etch
25	TRL	Photo wet sta- tion (non Au)	-	Acetone release
26	TRL	Asher	-	Strip P.R. / teflon



# Appendix B

## MASKS

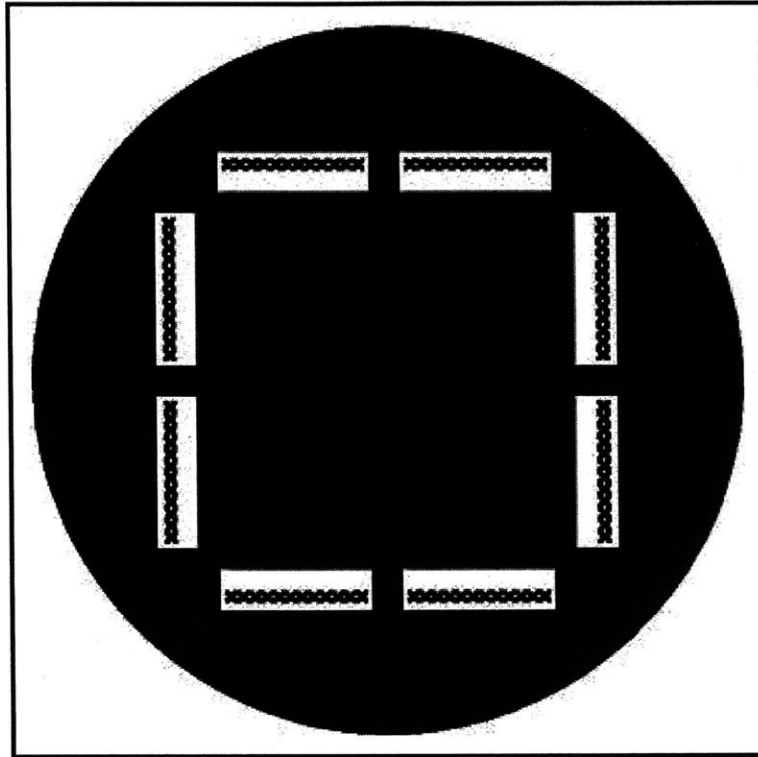


Figure B.1 Mask M-1

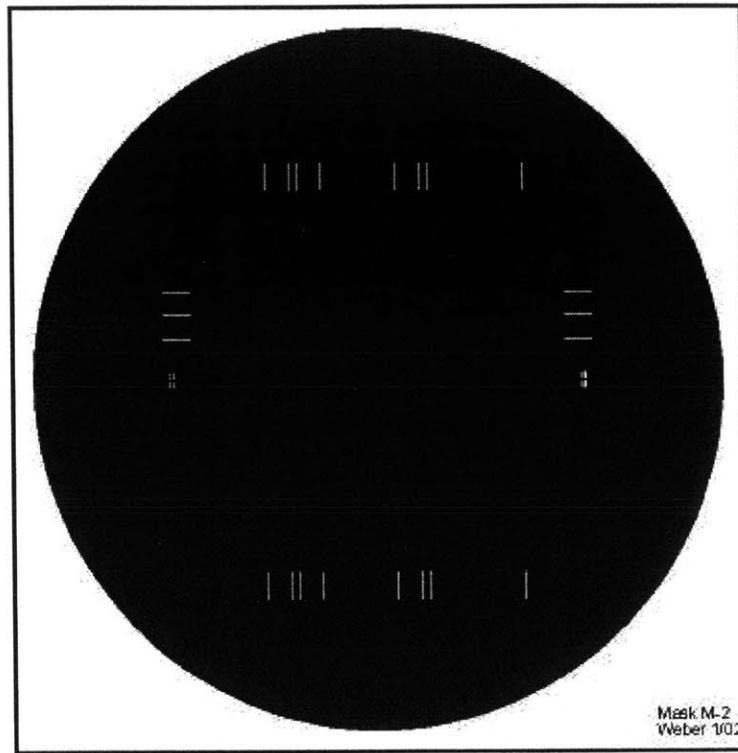


Figure B.2 Mask M-2

||

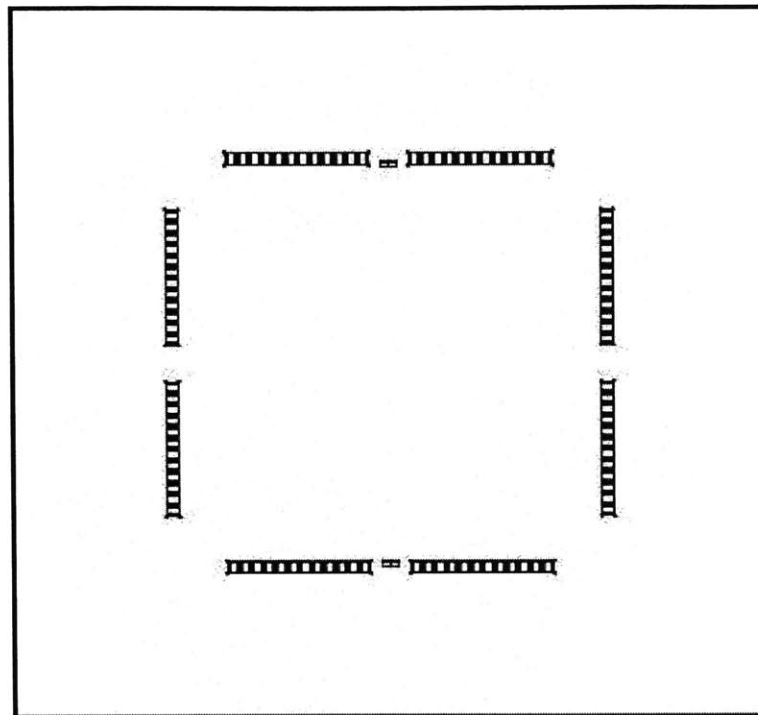
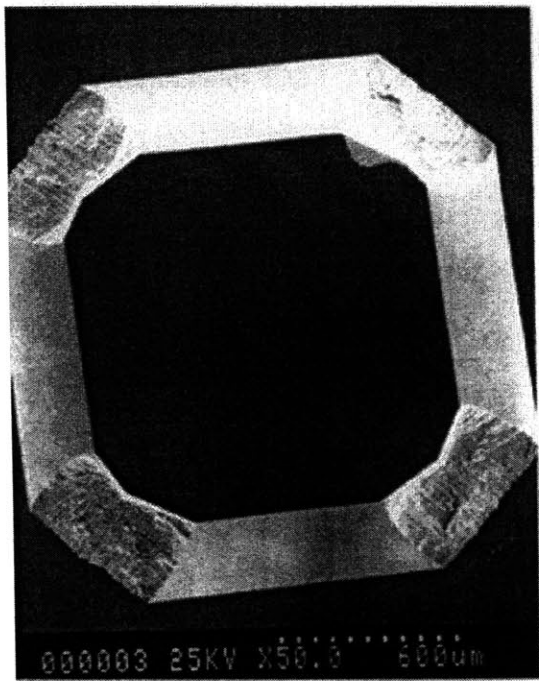


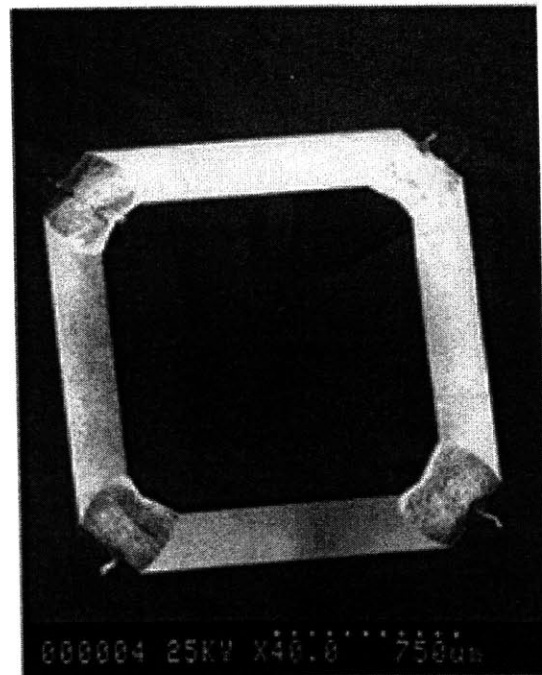
Figure B.3 Mask F

# Appendix C

## EXPERIMENTAL RESULTS: CCCS



**Figure C.1** CCCS optimization, die E1



**Figure C.2** CCCS optimization, die E2

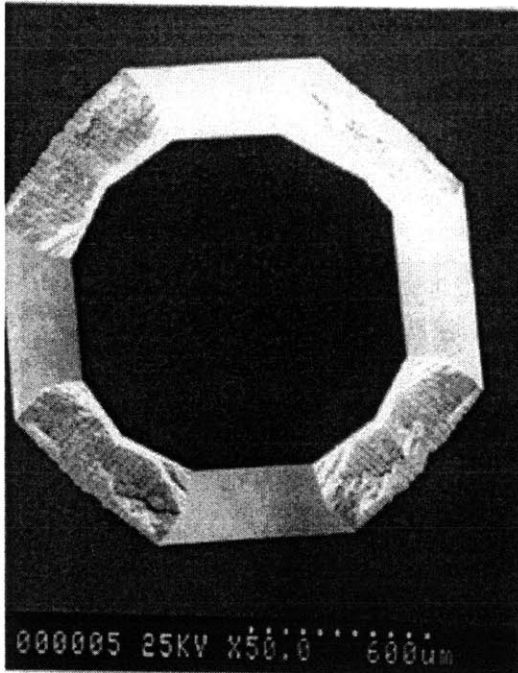


Figure C.3 CCCS optimization, die E3

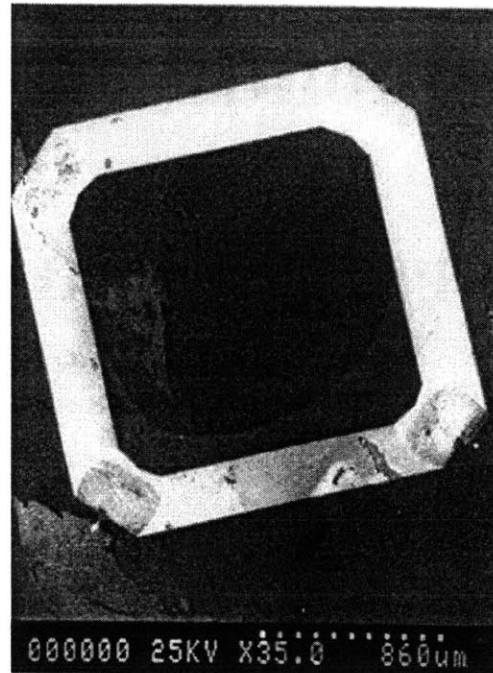


Figure C.4 CCCS optimization, die G1

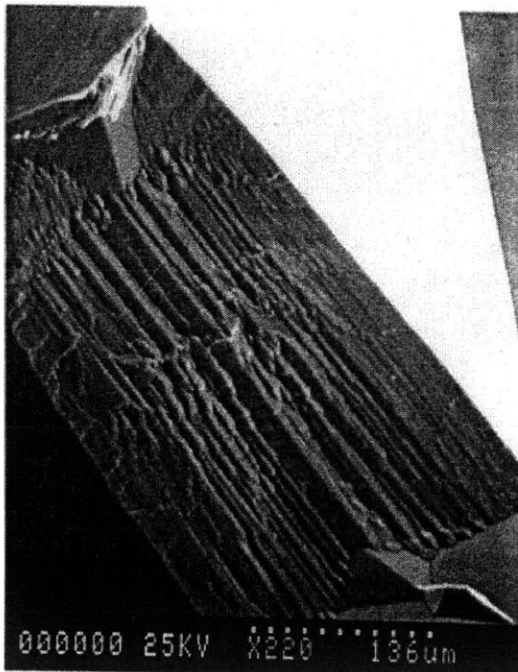


Figure C.5 CCCS optimization, corner detail die G1

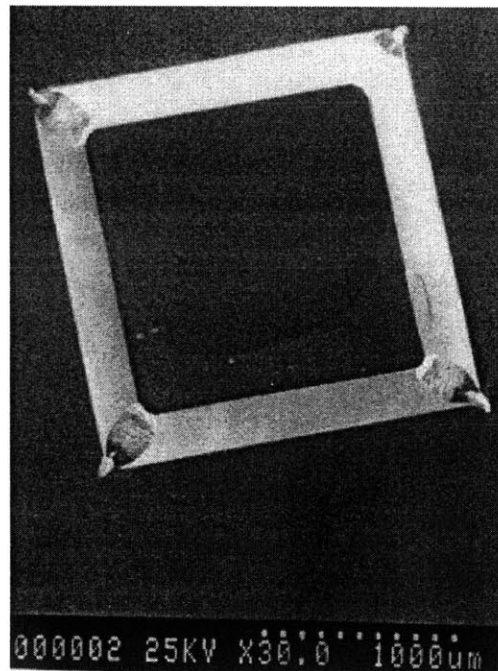


Figure C.6 CCCS optimization, die G2

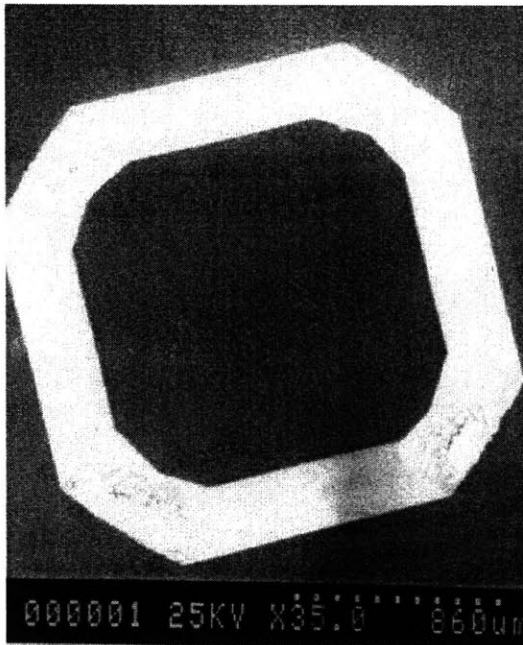


Figure C.7 CCCS optimization, die G3

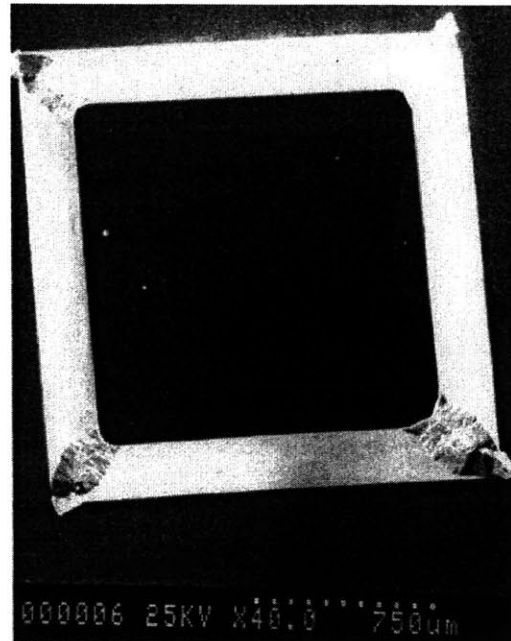


Figure C.8 CCCS optimization I1

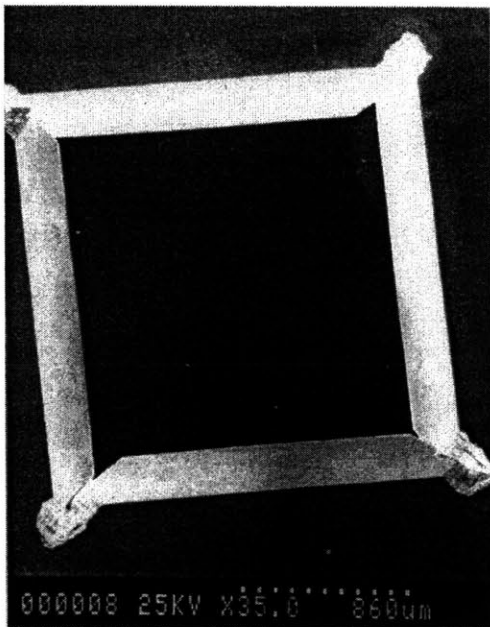


Figure C.9 CCCS optimization, die I2

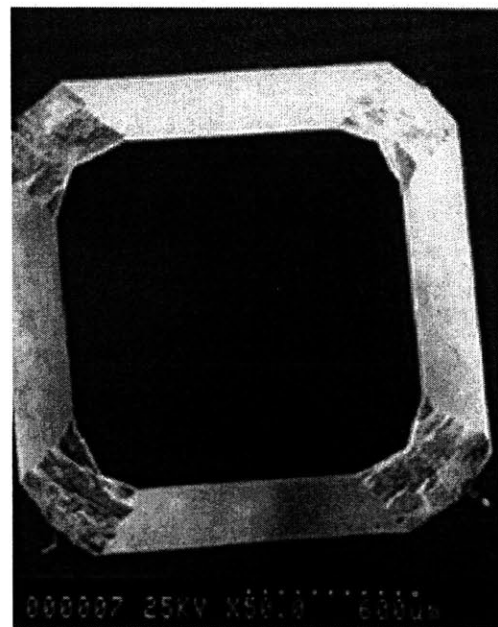


Figure C.10 CCCS optimization, die I3





# **Appendix D**

## **PASSIVE WAFER ALIGNMENT TEST DATA**

**TABLE D.1** Cap Test data, wafers M-1 & F-1 preloaded

Run	X [ $\mu\text{m}$ ]	Y [ $\mu\text{m}$ ]	Error [ $\mu\text{m}$ ]	Error Angle [deg]
1	0.42	-5.69	5.70	-85.77
2	0.21	-5.69	5.69	-87.88
3	0.42	-5.69	5.70	-85.77
4	0.21	-5.48	5.48	-87.8
5	0.21	-5.27	5.27	-87.71
6	0.21	-5.27	5.28	-85.44
7	0.21	-5.27	5.27	-87.71
8	0.21	-5.27	5.27	-87.71
9	0	-5.48	5.48	
10	0.42	-5.06	5.07	-85.25
11	0.21	-5.27	5.27	-87.71
12	0.42	-5.48	5.49	-85.61
13	0.63	-5.06	5.09	-82.90
14	0.42	-5.27	5.28	-85.44
15	0.42	-5.27	5.28	-85.44
16	0.42	-5.27	5.28	-85.44
17	0.42	-5.48	5.49	-85.61
18	0.42	-5.06	5.07	-85.25
19	0.42	-5.27	5.28	-85.44
20	0	-5.27	5.27	
21	0.42	-5.27	5.28	-85.44
22	0.84	-5.06	5.12	-80.57
23	0.84	-5.27	5.33	-80.94

**TABLE D.2** Test data Wafers M-2 & F-1, all cantilevers

Run	X [ $\mu\text{m}$ ]	Y [ $\mu\text{m}$ ]	Error [ $\mu\text{m}$ ]	Error Angle [deg]
1	1.26	-1.90	2.27	-56.44
2	1.05	-1.90	2.17	-61.07
3	0.84	-0.84	1.18	-44.99
4	1.05	-1.69	1.98	-58.14
5	0.84	-0.84	1.18	-44.99
6	1.05	-1.26	1.64	-50.19
7	0.63	-0.84	1.05	-53.13
8	1.26	-1.69	2.10	-53.19
9	0.69	-0.42	0.80	-31.32
10	0.84	-1.05	1.34	-51.34
11	0.84	-0.84	1.18	-44.99
12	0.84	-0.63	1.05	-36.86
13	0.63	-1.26	1.40	-63.43
14	0.84	-0.84	1.18	-44.99
15	1.05	-1.26	1.64	-50.19
16	0.84	-1.47	1.69	-60.25
17	1.05	-0.63	1.22	-30.96
18	0.42	-0.84	0.93	-63.43
19	0.63	-1.05	1.22	-59.03
20	0.84	-1.26	1.51	-56.30

**TABLE D.3** Test data wafers M-1 & F-1, no preload besides top wafer mass, 96 cantilevers

Run	X [ $\mu\text{m}$ ]	Y [ $\mu\text{m}$ ]	Error [ $\mu\text{m}$ ]	Error Angle [deg]
1	0.42	-5.48	5.49	-85.6
2	1.05	-5.69	5.78	-79.54
3	0.21	-5.48	5.48	-87.80
4	1.26	-5.48	5.62	-77.05
5	-0.42	-5.48	5.49	85.61
6	-0.63	-5.48	5.51	83.44
7	1.05	-5.90	5.99	-79.90
8	-0.63	-5.90	5.933	83.90
9	-1.68	-5.90	6.13	74.10
10	-0.21	-5.69	5.69	87.88
11	-0.63	-5.9	5.9	83.90
12	-1.05	-5.27	5.37	78.73
13	0.84	-5.69	5.75	-81.60
14	-1.26	-5.69	5.82	77.51
15	-1.68	-5.48	5.73	72.95

**TABLE D.4** Test data wafers M-1 & F-1, no preload besides top wafer mass, 88 cantilevers

Run	X [ $\mu\text{m}$ ]	Y [ $\mu\text{m}$ ]	Error [ $\mu\text{m}$ ]	Error Angle [deg]
1	-0.84	-5.90	5.95	81.89
2	-0.84	-5.69	5.75	81.60
3	1.05	-5.48	5.57	-79.15
4	-0.42	-5.90	5.91	85.92
5	0.21	-5.69	5.69	-87.88
6	1.05	-5.90	5.99	-79.90
7	-1.05	-5.48	5.57	79.15
8	1.88	-5.90	6.19	-72.32
9	-0.88	-5.96	6.24	72.49
10	1.47	-5.90	6.08	-76.00
11	1.68	-6.32	6.53	-75.11
12	-1.26	-5.69	5.82	77.51
13	-1.26	-5.69	5.82	77.51
14	-0.63	-5.48	5.51	83.44
15	-1.26	-5.69	5.82	77.51

**TABLE D.5** Test data wafers M-1 & F-1, no preload besides top wafer mass, 80 cantilevers

Run	X [ $\mu\text{m}$ ]	Y [ $\mu\text{m}$ ]	Error [ $\mu\text{m}$ ]	Error Angle [deg]
1	-0.84	-6.32	6.37	82.42
2	-0.42	-6.74	6.75	86.43
3	-0.63	-5.9	5.93	83.90
4	-0.63	-6.53	6.56	84.48
5	-0.42	-6.11	6.12	86.06
6	1.68	-5.9	6.13	-74.10
7	2.3	-6.32	6.72	-70.00
8	0	-5.9	5.90	0
9	2.09	-6.95	7.25	-73.26
10	2.3	-6.53	6.92	-70.59
11	2.3	-6.95	7.32	-71.68
12	2.72	-6.79	7.31	-68.16
13	2.51	-6.53	6.99	-68.97
14	2.72	-6.53	7.07	-67.38
15	2.30	-6.74	7.12	-71.15

**TABLE D.6** Test data wafers M-1 & F-1, no preload besides top wafer mass, 72 cantilevers

Run	X [ $\mu\text{m}$ ]	Y [ $\mu\text{m}$ ]	Error [ $\mu\text{m}$ ]	Error Angle [deg]
1	2.72	-6.53	7.07	-67.38
2	2.51	-6.74	7.19	-69.57
3	2.72	-6.53	7.07	-67.38
4	2.72	-6.74	7.26	-68.02
5	2.93	-6.74	7.34	-66.50
6	2.30	-6.95	7.32	-71.68
7	2.30	-6.95	7.32	-71.68
8	2.30	-6.74	7.12	-71.15
9	2.30	-6.74	7.12	-71.15
10	2.09	-6.95	7.25	-73.26
11	2.30	-7.37	7.72	-72.66
12	2.51	-7.16	7.58	-70.68
13	2.30	-7.16	7.52	-72.19
14	2.30	-7.16	7.52	-72.19
15	2.72	-7.16	7.65	-69.19

**TABLE D.7** Test data wafers M-1 & F-1, no preload besides top wafer mass, 64 cantilevers

Run	X [ $\mu\text{m}$ ]	Y [ $\mu\text{m}$ ]	Error [ $\mu\text{m}$ ]	Error Angle [deg]
1	-4.19	-10.32	11.13	67.90
2	-4.19	-9.69	10.55	66.61
3	-5.44	-9.90	11.29	61.21
4	-3.56	-9.69	10.32	69.82
5	-3.98	-9.90	10.67	68.09
6	-4.19	-9.90	10.75	67.06
7	-4.19	-9.48	10.36	66.15
8	-4.40	-9.20	10.19	64.43
9	-5.83	-9.48	11.14	58.27
10	-4.19	-9.69	10.55	66.61
11	-3.77	-9.69	10.39	68.74
12	-4.19	-10.32	11.13	67.90
13	-4.19	-10.11	10.94	67.48
14	-4.19	-9.69	10.55	66.61
15	-4.19	-9.90	10.75	67.06

**TABLE D.8** Test data wafers M-1 & F-1, no preload besides top wafer mass, 56 cantilevers

Run	X [ $\mu\text{m}$ ]	Y [ $\mu\text{m}$ ]	Error [ $\mu\text{m}$ ]	Error Angle [deg]
1	-3.98	-8.64	9.51	65.26
2	-3.98	-9.27	10.08	66.76
3	-4.19	-9.06	9.98	65.18
4	-4.19	-9.48	10.36	66.15
5	-3.98	-8.85	9.70	65.78
6	-4.19	-8.85	9.79	64.66
7	-4.19	-9.48	10.36	66.15
8	-4.4	-9.06	10.07	64.09
9	-4.4	9.06	10.07	64.09
10	-4.4	-9.06	10.07	64.09
11	-4.19	-8.85	9.79	64.66
12	-4.40	-9.06	10.07	64.09
13	-5.23	-8.43	9.92	58.18
14	-4.61	-9.00	10.11	62.87
15	-4.40	-9.06	10.07	64.09

**TABLE D.9** Test data wafers M-1 & F-1, no preload besides top wafer mass, 48 cantilevers

Run	X [ $\mu\text{m}$ ]	Y [ $\mu\text{m}$ ]	Error [ $\mu\text{m}$ ]	Error Angle [deg]
1	-2.93	-6.11	6.77	64.38
2	-5.65	-7.58	9.45	5.29
3	-5.44	-2.58	6.02	25.37
4	-5.23	-7.58	9.20	55.39
5	-5.44	-8.43	10.03	57.16
6	-5.44	-8.22	9.85	56.60
7	-5.03	-7.58	9.09	56.43
8	-5.23	-7.79	9.38	56.12
9	-5.44	-8.01	9.68	55.81
10	-5.03	-6.95	8.57	54.10
11	-5.86	-7.79	9.74	53.04
12	-5.23	-7.79	9.38	56.12
13	-5.78	-7.79	9.70	53.42
14	-5.65	-7.58	9.45	53.29
15	-5.86	-7.16	9.25	50.70

**TABLE D.10** Test data wafers M-2 & F-2. no preload besides wafer mass, 96 cantilevers

Run	X [ $\mu\text{m}$ ]	Y [ $\mu\text{m}$ ]	Error [ $\mu\text{m}$ ]	Error Angle [deg]
1	-6.91	1.90	7.16	-15.37
2	-6.91	1.90	7.16	-15.37
3	-6.49	1.26	6.61	-10.98
4	-7.54	1.26	7.64	-9.48
5	-6.70	1.26	6.81	-10.65
6	-7.33	1.26	7.43	-9.75
7	-6.91	1.26	7.02	-10.33
8	-7.12	1.42	7.26	-11.27
9	-7.12	1.47	7.27	-11.66
10	-7.12	1.26	7.23	-10.03
11	-6.91	1.90	7.16	-15.37
12	-6.28	1.42	6.43	-12.74
13	-7.37	1.69	7.56	-12.91
14	-6.91	0.21	6.91	-1.74
15	-6.07	1.26	6.19	-11.72

**TABLE D.11** Test data wafers M-2 & F-2. no preload besides wafer mass, 88 cantilevers

Run	X [ $\mu\text{m}$ ]	Y [ $\mu\text{m}$ ]	Error [ $\mu\text{m}$ ]	Error Angle [deg]
1	-6.28	1.05	6.36	-9.49
2	-6.7	0.84	6.75	-7.14
3	-6.07	0.63	6.10	-5.92
4	-6.70	0.84	6.75	-7.14
5	-6.28	0.84	6.33	-7.61
6	-6.28	0.84	6.33	-7.61
7	-6.28	0.63	6.31	-5.72
8	-5.88	0.27	5.88	-2.62
9	-6.28	0.63	6.311	-7.2
10	-5.86	0.63	5.89	-6.13
Average	-6.26	0.75	6.30	-6.51
Range	0.84	0.78	0.866	6.86

**TABLE D.12** Test data wafers M-2 & F-2. no preload besides wafer mass, 80 cantilevers

Run	X [ $\mu\text{m}$ ]	Y [ $\mu\text{m}$ ]	Error [ $\mu\text{m}$ ]	Error Angle [deg]
1	-6.91	0.42	6.92	-3.47
2	-6.91	0.42	6.922	-3.17
3	-7.54	0.42	7.55	-3.18
4	-6.91	0.21	6.91	-1.74
5	-6.99	0.21	6.99	-1.72
6	-7.33	1.05	7.40	-8.15
7	-7.33	0.63	7.35	-4.91
8	-7.54	0.84	7.58	-6.35
9	-7.54	0.21	7.54	-1.59
10	-7.75	0.21	7.75	-1.55
Average	-7.28	0.43	7.29	-3.61
Range	0.84	0.84	0.83	6.59



**TABLE D.13** Test data wafers M-2 & F-2. no preload besides wafer mass, 72 cantilevers

Run	X [ $\mu\text{m}$ ]	Y [ $\mu\text{m}$ ]	Error [ $\mu\text{m}$ ]	Error Angle [deg]
1	-2.09	4.63	5.07	-65.7
2	-1.26	4.00	4.19	-72.51
3	-1.68	4.63	4.92	-70.05
4	-1.88	4.42	4.80	-66.95
5	-1.88	4.85	5.20	-68.81
6	-1.05	4.63	4.74	-7.22
7	-1.68	4.85	5.13	-70.89
8	-1.68	4.63	4.92	-70.05
9	-1.88	4.00	4.19	-64.82
Average	-1.67	4.51	4.82	-69.67
Range	1.04	0.85	1.00	12.39

**TABLE D.14** Test data wafers M-2 & F-2. no preload besides wafer mass, 64 cantilevers

Run	X [ $\mu\text{m}$ ]	Y [ $\mu\text{m}$ ]	Error [ $\mu\text{m}$ ]	Error Angle [deg]
1	-4.19	-6.11	7.40	55.55
2	-4.19	-5.69	7.06	53.63
3	-4.61	-5.90	7.48	51.99
4	-4.19	-5.90	7.23	54.61
5	-4.19	-5.69	7.06	53.63
6	-4.18	-5.69	7.06	53.69
Average	-4.30	-5.85	7.22	53.85
Range	0.43	0.42	0.42	3.56

**TABLE D.15** Test data wafers M-2 & F-2. no preload besides wafer mass, 56 cantilevers

Run	X [ $\mu\text{m}$ ]	Y [ $\mu\text{m}$ ]	Error [ $\mu\text{m}$ ]	Error Angle [deg]
1	-5.86	-4.21	7.21	35.69
2	-5.86	-4.21	7.21	35.69
3	-6.28	-4.21	7.56	33.83
4	-5.86	-4.42	7.34	37.02
5	-5.86	-4.21	7.21	35.69
6	-6.28	-4.42	7.67	35.13
Average	-5.99	-4.26	7.37	35.51
Range	0.63	0.21	0.46	3.18

**TABLE D.16** Test data wafers M-2 & F-2. no preload besides wafer mass, 48 cantilevers

Run	X [ $\mu\text{m}$ ]	Y [ $\mu\text{m}$ ]	Error [ $\mu\text{m}$ ]	Error Angle [deg]
1	-6.7	-4.21	7.91	32.14
2	-6.70	-4.42	8.02	33.41
3	-6.49	-4.21	7.73	32.97
4	-6.70	-4.21	7.91	32.14
5	-6.49	-4.00	7.62	31.64
6	-6.70	-4.21	7.91	32.14
7	-6.70	-4.00	7.80	30.83
8	-6.07	-4.42	7.50	36.06
9	-6.28	-4.21	7.56	33.83
10	-6.70	-4.42	8.02	33.41
11	-6.70	-4.42	8.02	33.41
Average	-6.55	-4.21	7.82	32.91
Range	0.63	0.42	0.51	5.22

**TABLE D.17** Test data wafers M-2 & F-2. no preload besides wafer mass, 40 cantilevers

Run	X [ $\mu\text{m}$ ]	Y [ $\mu\text{m}$ ]	Error [ $\mu\text{m}$ ]	Error Angle [deg]
1	-6.28	-3.58	7.22	29.68
2	-6.28	-4.00	7.44	32.49
3	-6.49	-4.00	7.62	31.64
4	-6.28	-3.37	7.12	28.21
5	-6.70	-3.37	7.49	26.70
6	-6.28	-4.00	7.44	32.49
7	-6.28	-3.37	7.12	28.21
8	-6.70	-4.00	7.80	30.83
9	-6.49	-3.79	7.51	30.28
Average	-6.45	-3.68	7.42	30.06
Range	0.42	0.63	0.67	5.79

**TABLE D.18** Test data wafers M-2 & F-2. no preload besides wafer mass, 32 cantilevers

Run	X [ $\mu\text{m}$ ]	Y [ $\mu\text{m}$ ]	Error [ $\mu\text{m}$ ]	Error Angle [deg]
1	-4.40	-5.90	7.36	53.28
2	-5.03	-5.69	7.59	48.52
3	-5.03	-5.06	7.13	45.17
4	-4.40	-5.90	7.36	53.28
5	-4.40	-5.06	6.70	48.99
6	-4.61	-5.69	7.32	50.98
7	-4.82	-5.48	7.29	48.66
8	-4.82	-5.48	7.29	48.66
9	-4.61	-5.69	7.32	50.98
10	-4.40	-5.27	6.86	5.14
Average	-4.61	-5.43	7.22	49.87
Range	0.63	1.05	0.88	8.11

**TABLE D.19** Test data wafers M-2 & F-2. no preload besides wafer mass, 24 cantilevers

Run	X [ $\mu\text{m}$ ]	Y [ $\mu\text{m}$ ]	Error [ $\mu\text{m}$ ]	Error Angle [deg]
1	-8.17	-3.58	8.91	23.66
2	-7.75	-3.37	8.45	23.50
3	-7.75	3.58	8.53	24.79
4	-7.96	-3.58	8.72	24.21
5	-7.33	-3.79	8.25	27.34
6	-7.33	-4.42	8.55	31.08
7	-7.54	-4.21	8.63	29.17
8	-7.33	-4.42	8.55	31.08
9	-7.54	-4.00	8.53	27.94
10	-7.33	-3.79	8.25	27.34
11	-7.33	-4.00	8.35	28.62
<b>Average</b>	-7.55	-3.87	8.52	27.16
<b>Range</b>	0.84	1.05	0.66	7.58

**TABLE D.20** Test data wafers M-2 & F-2. no preload besides wafer mass, 16 cantilevers

Run	X [ $\mu\text{m}$ ]	Y [ $\mu\text{m}$ ]	Error [ $\mu\text{m}$ ]	Error Angle [deg]
1	-7.33	-4.42	8.55	31.08
2	-7.55	-4.85	9.14	32.03
3	-7.55	4.85	9.14	32.03
4	-7.33	-4.63	8.66	32.27
5	-7.33	-5.06	8.90	34.61
6	-7.33	-4.85	8.78	33.49
7	-7.33	-4.63	8.66	32.27
8	-7.54	-4.85	8.96	32.75
9	-7.75	-4.85	9.14	32.03
10	-7.54	-4.85	8.96	32.75
11	-7.54	-4.63	8.84	31.55
<b>Average</b>	-7.50	-4.76	8.89	32.44
<b>Range</b>	0.42	0.64	0.58	3.52

**TABLE D.21** Test data wafers M-2 & F-2. no preload besides wafer mass, 8 cantilevers

Run	X [ $\mu\text{m}$ ]	Y [ $\mu\text{m}$ ]	Error [ $\mu\text{m}$ ]	Error Angle [deg]
1	-7.33	-3.37	8.06	24.69
2	-7.33	-3.16	-7.8	23.32
3	-.91	-3.16	7.59	24.57
4	-7.33	-2.74	7.82	20.49
5	-6.91	-3.37	7.68	25.99
6	-7.33	-3.37	8.06	24.69
7	-7.33	-3.37	8.06	24.69
8	-7.12	-3.58	7.96	26.69
9	-6.91	-3.37	7.68	25.99
<b>Average</b>	-7.14	-3.19	7.88	24.57
<b>Range</b>	0.42	0.84	0.46	6.19

